UC Berkeley
UC Berkeley Previously Published Works

Title

A phospholipid mimetic targeting LRH-1 ameliorates colitis.

Permalink

Journal

Authors

Mays, Suzanne
DAgostino, Emma
Flynn, Autumn
et al.

Publication Date

DOI

Peer reviewed

A phospholipid mimetic targeting LRH-1 ameliorates colitis

Suzanne G. Mays[1,a,#], **Emma H. D'Agostino**[1,a], **Autumn R. Flynn**[2], **Xiangsheng Huang**[4,5], **Guohui Wang**[4,5], **Xu Liu**[1], **Elizabeth J. Millings**[1,3], **C. Denise Okafor**[1], **Anamika Patel**[1], **Michael L. Cato**[1], **Jeffery L. Cornelison**[2], **Diana Melchers**[6], **René Houtman**[6], **David D. Moore**[4,7], **John W. Calvert**[3], **Nathan T. Jui**[2,*], **Eric A. Ortlund**[1,b,*]

[1]Department of Biochemistry, Emory University, Atlanta, GA, USA;

[2]Department of Chemistry, Emory University, Atlanta, GA, USA;

[3]Department of Surgery, Emory University, Atlanta, GA, USA;

[4]Department of Molecular and Cell Biology, Baylor College of Medicine, Houston, TX, USA;

[5]Department of Pediatrics, Baylor College of Medicine and Texas Children's Hospital, Houston, TX, USA;

[6]Precision Medicine Lab, Oss, The Netherlands;

[7]Department of Nutritional Sciences and Toxicology, University of California, Berkeley, Berkeley CA, USA

Summary

Phospholipids are ligands for nuclear hormone receptors (NRs) that regulate transcriptional programs relevant to normal physiology and disease. Here, we demonstrate that mimicking phospholipid-NR interactions is a robust strategy to improve agonists of liver receptor homolog-1 (LRH-1), a therapeutic target for colitis. Conventional LRH-1 modulators only partially occupy the binding pocket, leaving vacant a region important for phospholipid binding and allostery. Therefore, we constructed a set of molecules with elements of natural phospholipids appended to a synthetic LRH-1 agonist. We show that the phospholipid-mimicking groups interact with the targeted residues in crystal structures and improve binding affinity, LRH-1 transcriptional activity, and conformational changes at a key allosteric site. The best phospholipid mimetic markedly improves colonic histopathology and disease-related weight loss in a murine T-cell transfer model

*Correspondence to: Eric A. Ortlund, eortlun@emory.edu, Nathan T. Jui, nathan.jui@gmail.com.
#Current address: Centre for Genomic Regulation, Calle del Doctor Aiguader 88, Barcelona, Spain
aThese authors contributed equally
bLead Contact: Eric A. Ortlund

of colitis. This evidence of *in vivo* efficacy for an LRH-1 modulator in colitis represents leap forward in agonist development.

Keywords

Phospholipid; LRH-1; nuclear receptor; agonist; ulcerative colitis

Introduction

Phospholipids (PLs) play many roles in physiology, such as forming lipid bilayers, signaling for apoptosis, and activating G-protein coupled receptors (Chaurio et al., 2009; Dawaliby et al., 2016; van der Veen et al., 2017). Phosphatidylcholines (PCs) are a subtype of PL vital for maintaining integrity and curvature of eukaryotic cellular membranes (Li et al., 2006) and for mediating cell signaling programs. Catabolism of PCs produces bioactive molecules, such as arachidonic acid (Furse and de Kroon, 2015), and generates labile methyl groups used for DNA methylation and synthesis of nucleotides and amino acids (Walker, 2017). Additionally, certain PCs exert broad effects on metabolic homeostasis by acting as ligands for nuclear hormone receptors (NRs)(Chakravarthy et al., 2009; Lee et al., 2011; Liu et al., 2013; Musille et al., 2013a; Musille et al., 2012). As NR ligands, PCs represent an understudied class of hormone.

Particularly strong evidence supports a role for PCs as ligands of liver receptor homolog-1 (LRH-1). LRH-1 is an orphan NR that regulates cholesterol homeostasis, metabolism, proliferation, and intestinal inflammation, garnering attention as a therapeutic target for diseases such as diabetes, cancer, and inflammatory bowel diseases (Bayrer et al., 2018; Cobo-Vuilleumier et al., 2018; Coste et al., 2007; Lee et al., 2011; Mamrosh et al., 2014; Nadolny and Dong, 2015; Xu et al., 2016). LRH-1 binds a wide range of PLs *in vitro*, and it is activated exogenously by medium-chained, saturated PCs (Lee et al., 2011; Musille et al., 2015). Moreover, several models have shown a relationship between endogenous PC levels and LRH-1 activity. Diet-induced depletion of PCs in mice induces an "antagonistic" pattern of gene expression in the liver similar to LRH-1 liver-specific knockout mice (Wagner et al., 2016). Similarly, diet-induced depletion of PCs in *C. elegans* inhibits the worm LRH-1 ortholog (Lin and Wang, 2017). In human hepatocytes, LRH-1 senses PCs generated via methyl metabolism to control beta-oxidation of fatty acids and mitochondrial biogenesis (Choi et al., 2019). Finally, a PC agonist of LRH-1 (dilauroylphosphatidylcholine, DLPC) induces LRH-1-dependent anti-diabetic effects in mouse models of insulin resistance (Lee et al., 2011). The anti-diabetic effects occur via repression of *de novo* lipogenesis in the liver.

The sensitivity of LRH-1 to PC levels suggests a regulatory circuit connecting PC availability to LRH-1-controlled gene expression. However, this circuit has been difficult to elucidate. Natural PCs are insoluble, rapidly metabolized, and unlikely to be LRH-1-selective, which makes them difficult to work with in the laboratory. These poor pharmacological properties also limit the use of PCs as therapeutics. We therefore designed a set of "PL-mimics" by fusing PL headgroups (or phosphate bioisosteres) to the synthetic LRH-1 agonist RJW100 (Figure 1A–B)(Flynn et al., 2018). These hybrid molecules

contain the hexahydropentalene (6HP) core from RJW100, appended with a polar moiety that mimics a PL headgroup at position R^4 (Figure 1A–B)(Flynn et al., 2018). Based on structural analyses, we hypothesized that the modified R^4 groups would mimic PL interactions in the LRH-1 binding pocket and stimulate receptor activity. Indeed, the agonists activate LRH-1 robustly *in vitro* and promote distinctive patterns of coregulator protein recruitment. We present crystal structures showing that the agonists are anchored deeply in the pocket via the 6HP core and that the added polar groups make PL-like contacts at the mouth of the pocket as designed. The best of this class is active *in vivo*, suppressing lipogenic genes in the liver and inducing steroidogenic genes in the gut in separate mouse studies. In a murine model of chronic colitis, the best PL-mimic profoundly reduces inflammation and disease-related weight loss. This work demonstrates that strategic targeting of the PC binding site improves activity, elucidates the mechanism of action of these compounds, and provides evidence of *in vivo* efficacy in colitis.

Results

Structure-guided design of PL-mimics.

We exploited information from LRH-1 crystal structures to design a set of synthetic PL-mimetics (Flynn et al., 2018; Mays et al., 2016; Musille et al., 2012; Ortlund et al., 2005; Sablin et al., 2015). NRs are transcription factors regulated by hormone ligands that can stimulate or repress transcriptional activity depending on the nature of the ligand and conformational changes it induces. PLs bind LRH-1 differently than most NR ligands: rather than being fully engulfed in the pocket, a portion of the headgroup protrudes into the solvent (Figure 1A). Lipid phosphates coordinate polar residues near the pocket mouth, while the acyl chains line the pocket interior, making numerous hydrophobic contacts (Figure 1A). In contrast, the synthetic LRH-1 agonist RJW100 binds deep in the pocket (Figure 1A). We previously focused on strengthening deep pocket interactions made by RJW100, resulting in the discovery of the agonists 6N and 6Na (Figure S1)(Cornelison et al., 2020; Mays et al., 2019). For the PL-mimics, we used an alternative approach, seeking to promote interactions near the mouth of the pocket. Notably, the alkyl "tail" of RJW100 (position R^4) overlaps with the PL fatty acyl chains and follows a trajectory toward the pocket mouth (Figure 1A). Based on this observation, we synthesized sets of compounds modified at R^4 with alkyl tails of varied lengths that terminate in polar, PL-mimicking groups (Figure 1B)(Flynn et al., 2018). We reasoned that extension of the hydrophobic tail would bring the PL-mimicking group in proximity to residues important for coordinating PL headgroups (*i.e.* G421, Y516, and K520, Figure 1A). This would allow the compounds to maintain important interactions in the deep pocket via the 6HP core while introducing PL-like interactions with the extended moiety.

Modifications improve binding affinity and activity.

The addition of a phosphorylcholine (ChoP) or carboxylic acid (CA) to position R^4 on the RJW100 scaffold increases LRH-1 transcriptional activity, dependent upon the length of the alkyl linker connecting the bicyclic core to the modified group (Flynn et al., 2018). Compounds containing linkers of 9–10 carbons are the strongest activators for both classes, increasing E_{max} nearly two-fold over RJW100 (Figure 1C). The optimal

linker is 18–20 Å from the bicyclic core to the terminal polar group for the ChoPs and 15–17 Å for the CAs (Figure 1C, Table S1). Compounds with short alkyl linkers (4–5 carbons) do not significantly activate the receptor above baseline at doses up to 30 μM. Diverse modifications elsewhere on the RJW100 scaffold (Mays et al., 2019) affect potency (EC_{50}) but rarely increase E_{max} (Figure 1D), demonstrating a unique ability for the R^4 modifications to increase activity levels. The PL-mimicking groups also improve binding affinity in a linker length-dependent manner (Figure 1F–G, Table S1). ChoPs and CAs with longer linkers (9–11 carbons) have the highest affinities, with K_i values between 2–11 nM (Figure 1E–G, Table S1). To test whether the improved affinity and activity are caused by the longer alkyl linker or the terminal polar group, we synthesized and tested a set of diols (terminally hydroxy-modified at R^4) with varying linker lengths (Figure 1B). Longer linkers do not improve binding or activity of the diols compared to RJW100, suggesting that the charged polar group causes the improvements (Figure 1D, 1G, Table S1). Together, these data suggest that PL-mimicking groups form productive interactions with LRH-1, greatly increasing transcriptional output. The charged group at R^4 also improves aqueous solubility, which is quite poor for RJW100 (cLogP = 7.9, Figure S1B). The cLogP values for the best of the PL-mimics are between −2.1 and 4.1. We confirmed cLogP trends empirically by measuring aqueous solubility for RJW100 and 9CA (representing a middle value in the cLogP range) using mass spectrometry (Figure S1B). In this assay, RJW100's solubility limit is 2.9 μM, while 9CA's is 51 μM. 9CA also exhibits greater microsomal stability *versus* RJW100 (Figure S1C).

Phospholipid mimetics make PL-like interactions in the LRH-1 binding pocket important for binding and activation.

To understand the mechanism of action of the PL-mimics, we determined X-ray crystal structures of the LRH-1 ligand binding domain (LBD) bound to either 10CA or 9ChoP at resolutions of 2.3 Å and 2.55 Å, respectively (Figure 2A–B, Table 1). Both structures depict the ligand bound at a single site in the ligand binding pocket (Figure 2A–B). In both structures, the peptide from the transcriptional intermediary factor 2 (Tif2) coregulator, added to stabilize the complexes, is bound at the activation function surface (AFS, comprised of portions of helices 3, 4, and the activation function helix (AF-H), Figure 2A–B).

The electron density surrounding 10CA and 9ChoP unambiguously indicates their positions in the ligand binding pocket, including the extended alkyl linkers and terminal polar groups (Figure 2C). The 6HP cores, styrene substituents and hydroxyl groups adopt nearly identical positions in the deep pocket to RJW100 (Figure S2A). The alkyl tails of both 10CA and 9ChoP extend toward the mouth of the pocket, with the terminal polar groups close to the DLPC phosphate (seen by superposition with PDB 4DOS, Figure 2D). The contacts made by the CA and ChoP groups near the mouth of the pocket are very similar to those made by DLPC, including hydrogen bonds with the sidechains of residues Y516 and K520, the -amino group of G421, as well as a water-mediated hydrogen bond with the -amino group of L424 (Figure 2E–F). Molecular dynamics simulations (MDS) with the 10CA structure show that the interactions with Y516 and K520 persist for 50.2% and 37.6% of a 1 μs simulation, respectively. Similarly, DLPC interacts for 49.4% of the time with Y516 and 33.2% with

K520. The interaction with the backbone amide of G421 is less stable for 10CA than DLPC (27.0% of the simulation *versus* 48.1% for DLPC).

We were particularly interested in how the PL-mimics affect receptor conformation near the mouth of the pocket, since flexibility there is important for allosteric signaling by DLPC (Musille et al., 2015). PL binding expands the pocket mouth relative to apo LRH-1 via a ~3 Å displacement of helix 6 by the sn1 acyl chain (Mays et al., 2016; Musille et al., 2012). Helix 6 flexibility has been linked to allosteric communication between the ligand and the AFS (Musille et al., 2015). 10CA and 9ChoP do not shift helix 6; instead, they displace the C-terminus of helix 10 by 2.0–2.3 Å relative to apo LRH-1 (from superposition with PDB 4PLD) and 3.5–3.9 Å relative to the LRH-1-DLPC structure (Figure S2B).

To interrogate the function of the PL-like interactions made in the structures, we mutated key LRH-1 residues and measured the impact on binding affinity and transcriptional activity. Introduction of either a Y516A or K520A mutation decreases binding affinities of longer-tailed CAs and ChoPs by 14–60-fold *versus* WT LRH-1, with the exception of 9ChoP for the K520A mutation (Figure 2G, S3). The mutations also impair DLPC binding, decreasing its affinity by 24–40-fold (Figure 2G). Compounds with the 6HP scaffold that do not contact these residues (RJW100 and 6N)(Mays et al., 2019; Mays et al., 2016) are insensitive or less sensitive to these mutations (Figure 2G–H). In luciferase reporter assays, mutations to Y516A or K520A do not affect basal activity of LRH-1; however, the Y516A mutation reduces activation by all four agonists by 24–33% relative to WT protein (Figure 2I). Compounds 9CA and 10CA are very poor activators of the K520A mutant, reducing its activation by around 60% *versus* WT LRH-1, while 9ChoP and 10ChoP activate it equally well as WT protein. Therefore, one or more of the interactions near the mouth of the pocket contribute to the increased affinity and efficacy conferred by the extended polar group at R^4.

Longer-tailed PL mimetics stabilize the AFS and alter coregulator binding.— To understand how the PL-mimics switch LRH-1 into the active state, we investigated how activating *versus* non-activating CAs affect LRH-1 conformation in solution using hydrogen-deuterium exchange mass spectrometry (HDX-MS). We used four CAs for HDX-MS, two that bind LRH-1 but are inactive (4CA and 5CA) and the two most active agonists in this series (9CA and 10CA). Relative to the inactive compounds, 9CA and 10CA stabilize the LRH-1 activation function surface (AFS), the binding site for coregulator proteins (Figure 3A, Figure S4). Stabilized regions in the AFS include helix 3 and the loop preceding the activation function helix (pre-AF-H loop) (Figure 3A–C). 10CA also stabilizes the AF-H and part of helix 4 relative to 4CA (Figure 3A–B).

The stabilization of the AFS observed with HDX-MS suggests that 9CA and 10CA may affect coregulator associations. To test this, we conducted coregulator profiling using the Microarray Assay for Real-time Coregulator-Nuclear Receptor Interactions (MARCoNI), a microarray that quantifies associations of 64 coregulators from a library of 154 peptides containing NR interaction motifs (Koppen et al., 2009). We first investigated how long-*versus* short-tailed compounds affect coregulator binding to purified LRH-1 LBD, using the same CAs as the HDX-MS experiments. Since LRH-1 copurifies with PL from *E. coli* in the pocket, thought to act as weak agonists (Musille et al., 2015; Musille et al., 2012; Ortlund

et al., 2005) , we generated apo LRH-1 LBD by stripping the *E.* coli PL and refolding the receptor (Musille et al., 2012)(Figure S5). Apo LRH-1 LBD preferentially binds peptides from known LRH-1 corepressors (*i.e.*, nuclear receptor corepressor 1 (NCOR1), nuclear receptor subfamily 0 group B member 1 (NR0B1, also called DAX-1), and nuclear receptor subfamily 0 group B member 2 (NR0B2, also called SHP) (Figure S5). The strongest interactor is NFKB inhibitor beta (I B), a direct repressor of the retinoid X receptor (Na et al., 1998) that has not been previously reported to bind LRH-1 (Figure S5). Both 9CA and 10CA disrupt many of the strongest coregulator interactions with apo-LRH-1 (*i.e.*, I B , NCOR1, and transcriptional cofactor of c-*fos* (TREF1)), while strongly recruiting a specific complement of coregulators (*e.g.*, ligand dependent nuclear receptor corepressor (LCOR), nuclear receptor coactivator A1 (NCOA1) and nuclear receptor coactivator A3 (NCOA3), Figure 3D, S5). In contrast, 4CA and 5CA have much weaker effects on coregulator associations (Figure 3D, S5). Therefore, longer-tailed agonists promote conformational changes to the LBD that affect coregulator recognition of the AFS, consistent with observations from HDX-MS.

In addition to demarking differences between active and inactive compounds, the coregulator recruitment pattern of 9CA and 10CA also differs from that of 6N and 6Na, LRH-1 agonists that share the 6HP scaffold but are modified elsewhere on the molecule (Figure S1) (Cornelison et al., 2020; Mays et al., 2019). Unsupervised hierarchical clustering of the data shows a striking separation by ligand class: the most structurally similar ligands cluster together (Figure 3D). The close relationship between 9CA and 10CA in the clustering analysis appears to be due to common effects on coregulator dissociations. This distinguishes them from 4CA, which exhibits an otherwise similar (albeit weaker) pattern of coregulator associations to the longer-tailed compounds (Figure 3D). Coregulator recruitment by 6N and 6Na is also weak relative to the longer-tailed CAs, but it also displays a different pattern. For example, 9CA and 10CA promote dissociation of 16 coregulator peptides in common, while 6N and 6Na affect a distinct set of five coregulator peptides (Figure 3E).

Many of the observations from the experiment with isolated LBD are recapitulated in a MARCoNI study with FL-LRH-1. Since apo-FL protein was unstable, we used FL-LRH-1 bound to copurifying *E. coli* PL, which was found to have a nearly identical coregulator binding pattern to apo-LBD (Figure S5). FL-LRH-1 also responds very similarly to 10CA, recruiting peptides from LCOR, NCOA1, and SHP and dissociating I B , NCoR1, and TREF (Figure S5). In total, 85% of the peptides affected by at least 1.5-fold over baseline by 10CA in the LBD experiment are also altered by more than 1.5-fold with FL-LRH-1 (Figure 3F). Differences between 10CA and 6N are more apparent with FL-LRH-1 than LBD: 22 peptides are recruited by one compound and displaced by the other (Figure 3G). Together, these results demonstrate that receptor allostery is tunable through ligand modifications and reveal the importance of the PL-mimicking group in driving coregulator recruitment.

10CA reduces lipogenic gene expression in the liver.

LRH-1 is highly expressed in the liver, where it regulates bile acid biosynthesis, ER-stress resolution, and *de novo* lipogenesis (Lee et al., 2011; Lu et al., 2000; Mamrosh et al.,

2014). We tested whether 10CA, one of the most active of the PL-mimics, could activate endogenous LRH-1 in Huh7 hepatocytes. A 24-hour treatment of 10CA dose-dependently upregulates known LRH-1 transcriptional targets SHP (*NR0B2*) and polo-like kinase 3 (*PLK3*). 10CA also downregulates targets involved in *de novo* lipogenesis, including sterol regulatory element binding transcription factor 1 (*SREBF1*, also called *SREBP1-c*), acetyl-CoA carboxylase 2 (*ACACB*), fatty acid synthase (*FASN*), and stearoyl-CoA desaturase-1 (*SCD1*) (Figure 4A). Interestingly, downregulation of these lipogenic genes in the liver is associated with LRH-1-dependent antidiabetic effects by DLPC (Lee et al., 2011).

To determine whether 10CA can activate LRH-1 in the liver *in vivo*, we overexpressed human LRH-1 (hLRH-1) in C57BL/6J mice using AAV8 adenovirus. The overexpression strategy was chosen because 10CA and analogs are poor activators of mouse LRH-1 *in vitro*. Two weeks after viral infection, mice were treated with 10CA at 0.1, 1, or 10 mg/kg in a series of five intraperitoneal injections spanning three days (Figure 4B). Expression of hLRH-1 was verified by qRT-PCR (Figure 4C), and agonist-induced gene expression changes in the liver were assessed by Nanostring (Geiss et al., 2008). The most prominent effect of 10CA treatment is the downregulation of lipogenic genes (Figure 4D–E, Table S2). The affected genes are the same as those downregulated in Huh7 cells (*Fasn, Acacb,* and *Scd1*). *Srebf1* also trends lower in 10CA-treated mice but does not reach statistical significance (p = 0.09 *versus* vehicle-treated controls, Table S3). Expression of hLRH-1 is required for downregulation of the lipogenic genes, since their expression is unaffected in control mice given AAV8-GFP (p = 0.31 by two-way ANOVA).

Efficacy of 10CA in organoid and murine models of colitis.

To explore the efficacy of 10CA in a disease context, we tested it in models of intestinal inflammation and of ulcerative colitis, a chronic disease characterized by inflammation of the colon and decreased integrity of the intestinal epithelium (Ordás et al., 2012). LRH-1 is a therapeutic target for ulcerative colitis: it regulates local glucocorticoid production in the intestine, which is important for maintenance of the intestinal epithelial barrier (Bayrer et al., 2018; Bouguen et al., 2015; Coste et al., 2007; Mueller et al., 2006). Loss of LRH-1 function in mice decreases glucocorticoid production in the intestinal epithelium and decreases expression of *Cyp11a1* and *Cyp11b1*, genes that regulate corticosterone production (Coste et al., 2007). These defects are rescued by overexpression of hLRH-1 (Bayrer et al., 2018).

We first tested 10CA in organoids derived from intestinal crypts of mice, in which hLRH-1 is expressed in the context of conditional deletion of endogenous LRH-1 in the intestinal epithelium. These intestinal organoids (enteroids) mimic intestinal inflammation when stimulated with tumor necrosis factor alpha (TNF) (Basak et al., 2017; Bayrer et al., 2018; Mays et al., 2019). Overnight treatment with 10CA induces expression of *Cyp11a1* and the anti-inflammatory cytokine *Il-10* (Figure 5A). These changes in gene expression require the expression of hLRH-1, since they are not observed in epithelium-specific LRH-1-deficient enteroids (Figure 5A).

We used a naïve CD4+ T cell transfer (TCT) model of ulcerative colitis to test 10CA *in vivo*. In this model, immuno-compromised mice are implanted with naive T cells

(CD4$^+$CD45RB^{hi}) to induce intestinal inflammation and destruction of the intestinal epithelium in a gradual manner that resembles chronic colitis (Ostanin et al., 2009). Mice used in this experiment were generated by crossing recombinase activating gene-2-deficient (Rag2$^{-/-}$) mice with hLRH-1 mice (expressing hLRH-1 but not endogenous Lrh-1 in the intestinal epithelium (Ostanin et al., 2009)). Three weeks after T cell transfer, mice (n = 5) were treated with 10CA (20 mg/ kg) or vehicle (CTRL, 0.09% normal saline) for 16 days via intraperitoneal injections. Vehicle-treated animals lost an average of 8.6% initial body weight over the course of treatment, while mice treated with 10CA were protected from weight loss and were within 1% of mean pre-treatment body weights at the end of the study (Figure 5B). 10CA-treated mice also had markedly improved colon histology scores, which quantify severity of inflammation, tissue damage, and crypt loss in the colon (Figure 5C). Representative colonic tissue sections illustrate the striking differences between 10CA-treated and control mice (Figure 5D–E). Colonic crypts isolated from 10CA-treated mice showed strong upregulation of LRH-1 transcriptional targets, including *Cyp8b1*, *Cyp11a1*, and *Cyp11b1* (Figure 5F). This evidence of *in vivo* efficacy in a model of ulcerative colitis, demonstrates the potential of PL-mimicking LRH-1 agonists for treatment of inflammatory bowel diseases.

Discussion

The discovery that PCs act as NR ligands has illuminated the potential for the existence of signaling axes connecting PC metabolism with gene expression. Compelling evidence from gain- and loss-of-function studies connects PC availability to LRH-1-controlled transcriptional programs involving lipid and methyl metabolism. The response of LRH-1 to dietary PCs suggests that LRH-1 senses PCs as a proxy for nutrient availability, but this has been difficult to study. Likewise, PCs have anti-inflammatory effects in the intestinal mucosa that are not fully explained by their physical role in this tissue (Chen et al., 2017; Olson et al., 2014; Schneider et al., 2010; Treede et al., 2007). The agonists described herein provide tools to probe a potential LRH-1-PC regulatory circuit, which has been challenging to elucidate with natural PCs due to their lability and promiscuity (MacDonald, 1991).

Crystallographic data reveals very different binding modes of natural PL and the synthetic LRH-1 modulator RJW100, with the former making polar interactions near the mouth of the pocket and the latter being anchored in the deep pocket (Mays et al., 2016; Musille et al., 2012). The hybrid PL-mimics were designed with the rationale that appending a polar moiety to an extended R^4 alkyl tail would allow the agonists to interact with both regions of the pocket. With two crystal structures, we demonstrate that this strategy was successful: the 6HP cores nearly perfectly superpose with RJW100, while the polar groups in the extended tails form hydrogen bonds with several residues engaged by the DLPC phosphate group (Figure 2). Disrupting these hydrogen bonds via mutagenesis reduces binding affinity and decreases activity of the longer-tailed agonists (Figure 2). Compounds with shorter tails or lacking a charged group at the R^4 terminus are not more active than RJW100, further demonstrating that the PL-mimicking interactions are responsible for the improved binding and activity profiles (Figure 1). HDX-MS experiments show that the longer-tailed CAs stabilize the LRH-1 AFS relative to shorter-tailed CAs (Figure 3). AFS stabilization is associated with much stronger effects on coregulator recruitment than

seen with shorter-tailed CAs, including dissociation of many factors bound by apo-LRH-1 (Figure 3). Together, these data suggest a model in which specific interactions made by the PL-mimicking group promote conformational changes at the AFS that activate the receptor by modulating coregulator associations. Notably, the conformational changes induced by PL-mimics are different than DLPC, which expands the binding pocket via displacement of helix 6 (Musille et al., 2012). The PL-mimics do not displace helix 6 in the crystal structures; therefore, they mimic PC interactions but act more as hybrids between PCs and synthetic agonists with respect to receptor conformation. Nevertheless, the PL-mimics recapitulate many gene expression changes made by exogenous DLPC (Lee et al., 2011), including downregulation of lipogenic genes in hepatocytes and mouse liver (Figure 4). Downregulation of the same lipogenic genes and consequent suppression of *de novo* lipogenesis is thought to be the main mechanism through which DLPC exerts anti-diabetic effects, including reducing liver fat accumulation and improving insulin resistance (Lee et al., 2011). This suggests a potential for this agonist in diabetes and metabolic disorders associated with obesity, an ongoing area of research in our laboratories. A limitation of the mouse study with AAV8-hLRH-1 is that it is an overexpression model. Expression of the human receptor was needed due to amino acid differences in the binding pocket of the mouse homolog that reduce sensitivity to ligands (Musille et al., 2013b). However, hLRH-1 overexpression could increase basal activity, potentially blunting the effects of agonists. Future studies will address this limitation by utilizing a humanized mouse.

In addition to demonstrating the mechanism of action of the PL-mimics, the crystal structures presented herein suggest avenues for further improvement of LRH-1 agonists. The sulfamide modification in compound 6N improves potency in luciferase assays and engages a different part of the pocket than the PL-mimicking groups (Mays et al., 2019). The idea of combining the 10CA modification with the sulfamide is attractive. Based on the MARCoNI results (Figure 3), the two modifications may have some opposing effects on coregulator recruitment, which may affect transcription. Studies with a 6N-10CA hybrid molecule are currently underway in our laboratory to investigate this.LRH-1 is a therapeutic target for ulcerative colitis due to its role as a regulator of intestinal cell renewal and local inflammation in the gut (Bayrer et al., 2018; Mueller et al., 2006). One of the most exciting findings in these studies is the strong efficacy in ulcerative colitis *in vivo*. While gain and loss of function studies have demonstrated the potential of targeting LRH-1 in colitis (Bayrer et al., 2018), and the agonist 6N activates steroidogenic genes in enteroids (Mays et al., 2019), we show here that a synthetic LRH-1 agonist exhibits *in vivo* efficacy. In a TCT model of ulcerative colitis, 10CA decreases disease markers, inhibits colonic crypt loss, and ameliorates disease-associated weight loss, with concomitant changes in expression of LRH-1 controlled steroidogenic genes (Figure 5). Targeting LRH-1 in ulcerative colitis is a particularly intriguing strategy, as its activation suppresses inflammation locally in the gut (Fernandez-Marcos et al., 2011; Mueller et al., 2006). Ulcerative colitis is commonly treated with corticosteroids, anti-TNFα therapies, or other systemic immunosuppressants that often cause adverse effects associated with immunosuppression in tissues other than the colon (Gensler, 2013). Thus, LRH-1 agonists may offer a more precise approach to ulcerative colitis treatment, reducing the potential for on-target, adverse effects in other tissues.

This work has demonstrated an exciting potential for incorporating PL-mimicking interactions into LRH-1 agonists; however, there are some limitations to the study. First, the selectivity of 10CA for LRH-1 over related NR has not been evaluated. The gene expression changes and efficacy for 10CA are LRH-1-dependent, because they require the expression of human LRH-1 (Figure 1, 4–5). However, this does not rule out the possibility that the agonists also indirectly affect LRH-1 by binding another NR. An additional limitation is that we have not yet conducted *in vivo* pharmacokinetics studies with 10CA, which will be needed to optimize the dose and route of delivery for future experiments. Microsomal stability for a representative molecule in this class is rather low (Figure S1), suggesting that it will have a high clearance rate and short half-life *in vivo*. This could be considered a limitation or an asset depending on the application. For example, a compound with a short half-life given orally may act in the gut with limited systemic exposure. This may be beneficial for treatment of ulcerative colitis but may not be ideal for achieving high concentrations in the liver.

Together, these studies demonstrate that the PL-mimics are valuable tools to study LRH-1 activation by ligands and to broaden our understanding of PL-regulated transcriptional programs. They also have potential as therapeutics for diseases associated with aberrant LRH-1 activity.

STAR Methods

RESOURCE AVAILABILITY

Lead contact

- Further information and requests for resources and reagents should be directed to and will be fulfilled by the lead contact, Eric Ortlund (eortlun@emory.edu)

Materials availability

- Plasmids generated in this study are available upon request from the lead contact.

- Chemicals generated in this study are available upon request from the lead contact, subject to availability. Some chemicals may not be available due to small quantities synthesized.

Data and code availability

Data

- Coordinates and structure factors for x-ray crystal structures have been deposited at RCSB Protein Databank and are publicly available as of the date of publication. Accession numbers are listed in the key resources table.

- All data reported in this paper will be shared by the lead contact upon request

Code

- This paper does not report original code.

- Any additional information required to reanalyze the data reported in this paper is available from the lead contact upon request.

EXPERIMENTAL MODEL AND SUBJECT DETAILS

Animals—Experimental protocols for the AAV8-LRH-1 overexpression study were approved by the Institute for Animal Care and Use Committee at T3 Laboratories and Emory University and conformed to the Guide for the Care and Use of Laboratory Animals, published by the National Institutes of Health (NIH Publication No. 86–23, revised 1996), and with federal and state regulations. C57BL/6J mice (male; 10–12 weeks of age) were purchased from Jackson Labs (Bar Harbor, ME, USA). Mice were housed at room temperature in a 12-hr light/12-hr dark vivarium, with *ad libitum* access to food and water.

For the experiments involving enteroids and T-cell transfer, the study protocol was approved by the Animal Care and Use Committee of the Baylor College of Medicine and was in accordance with the Guide for the Care and Use of Laboratory Animals [DHHS publication no. (NIH) 85–23, revised 1985, Office of Science and Health Reports, DRR/NIH, Bethesda, MD 20205]. Animals were housed and bred in a specific pathogen free (SPF) facility. An inducible intestinal epithelial cell (IEC) knockout line was created by crossing animals harboring CreERT2 under control of the villin promoter with LRH-1 floxed (LRH-1$^{f/f}$) animals and bred to homozygosity (LRH-1 KO, LRH-1$^{f/f}$;Villin-Cre+). The humanized LRH-1 line (LRH-1$^{f/f}$;hLRH-1 ;Villin-Cre+) was generated with Rosa26-LoxP-STOP-LoxP-hLRH-1 animals, crossed into our LRH-1 KO line, which conditionally overexpresses hLRH-1 in the intestinal epithelium with the knockout of endogenous mLRH-1. The *hLRH1^{IEC} (Rag2$^{-/-}$ hLRH1^{IEC-TG}* mLRH1^{IEC-KO}) mouse line was generated by crossing *Flox-Stop-Flox hLRH-1;VilCre* animals with *Rag2$^{-/-}$ mLRH1$^{flox/flox}$;VilCre* animals *(hLRH1^{IEC})* animals, in which human LRH-1 replaces mouse LRH-1 in enterocytes.

For all mouse experiments, animals were test- and drug-naïve, and mice were randomized into experimental groups. Further experimental details are below in the section "Method Details."

Microbe strains—Competent *E. coli* strains BL21 DE3 and PlysS were purchased from Agilent. See information in Key Resources Table.

Cell lines—Huh7 cells (RRID:CVCL_0336) were provided by the Paul Dawson laboratory (Emory University) and cultured in DMEM/F12 medium supplemented with 10% FBS. Hela cells (RRID:CVCL_0058) were purchased from Atlantic Type Culture Collection (ATCC) and cultured in MEMα medium supplemented with 10% charcoal-stripped fetal bovine serum (FBS). Both cell lines were authenticated by ATCC. Cells tested negative for mycoplasma. Cells were cultured at a temperature of 37C, with 5% CO_2 and ~95% humidity.

METHOD DETAILS

Reporter gene assays.—Hela cells were seeded into white-walled, 96-well culture plates at 7500 cells/well. The next day, cells were transfected with reporter plasmids and

either pCI empty vector or full-length LRH-1-pCI (5 ng/well). Reporter plasmids consisted of (1) the pGL3 basic vector containing a portion of the SHP promoter containing the LRH-1 response element cloned upstream of firefly luciferase (50 ng/ well) and (2) a constitutively active vector encoding *Renilla* luciferase used for normalization (1 ng/ well). Transfections utilized the FugeneHD transfection reagent at a ratio of 5 µl Fugene: 2 µg DNA. Cells were treated with agonists 24 hours after transfection at concentrations indicated in the figure legends. Luminescence was quantified 24 hours after treatment using the DualGlo kit (Promega) on a BioTek Neo plate reader. EC_{50} and E_{max} were calculated by fitting data to a three-parameter dose-response curve.

Calculation of relative efficacy (RE).—RE was calculated to compare data from luciferase reporter assays conducted on different dates by normalizing to data from RJW100 assessed in parallel experiments. We used the formula $(Max_{cpd} - Min_{cpd}) / (Max_{RJW100} - Min_{RJW100})$. "Cpd" denotes the test compound, and "Max" and "Min" denote the dose response curve maximum and minimum, respectively. A RE of 0 indicates a completely inactive compound, a value of 1 indicates equal activity to RJW100, and values above 1 indicate greater activity.

Solubility assays.—cLogP values were calculated using ChemDraw Professional, v.18.0. The measure of aqueous solubility by liquid chromatography mass spectrometry (LC-MS) was conducted by Pharmaron, Inc (Louisville, KY). Compounds were assessed in duplicate. Test compounds (10 mM in DMSO) were diluted in PBS (pH 7.4) by addition of 30 µl of the DMSO stocks to 970 µl PBS in separate wells of an assay plate. The assay plate was transferred to an Eppendorf Thermomixer Comfort plate shaker and shook at 25°C at 1100 RPM for 2 hours. After completion of the 2 hours, the samples from the Solubility Sample plate were transferred into the filter plate. Using the Vacuum Manifold, all the samples were filtered. An aliquot of 10 µL was taken from the filtrate followed by addition of 990 µL of acetonitrile. A certain proportion of ultrapure water was used to dilute the diluent according to the peak shape. The dilution factor was changed according to the solubility values and the LC-MS signal response. The plate was placed into the well plate autosampler for analysis by LC-MS/MS using a Simadzu LC system and a Triple Quad™ 5500 MS instrument from Applied Biosystems, Inc. The filtrate was analyzed and quantified against a standard of known concentration using LC coupled with mass spectral peak identification and quantitation. Solubility values of the test compound and control compound were calculated as follows:

$$[Sample] = \frac{AREA_{Sample} \times INJVOL_{Std} \times DF_{Sample} \times [STD]}{AREA_{Std} \times INJVOL_{Sample}}$$

Microsomal stability.—Assays were conducted by Pharmaron, Inc (Louisville, KY). Reactions were carried out in 400 µl volumes. First, a master solution containing 100 mM phosphate buffer, 5 mM $MgCl_2$, 25 µg/ ml alamethicin, and 0.5 mg/ ml mouse liver microsomes was prepared and placed in reaction wells at a volume of 318 µl. Forty µL of 10 mM NADPH and 40 µL of 20 mM uridine diphosphate glucuronic acid (UDPGA) were added to each well to have final concentrations of 1 mM NADPH and 2 mM UDPGA.

Negative controls contained the master solution but substituted ultrapure water for NADPH and UDPGA cofactors. Reactions were started by addition of 2 μL of test compounds (RJW100 or 9CA) at final concentrations of 2 μM. Verapamil was used as a positive control (also used at 2 μM). Reactions containing test compounds with cofactors were conducted in duplicate, and negative control reactions were conducted without replicates. Aliquots of 50 μL were taken from the reaction solution at 0, 15, 30, 45 and 60 minutes. The reaction was stopped by the addition of 4 volumes of cold acetonitrile with internal standards (100 nM alprazolam, 200 nM imipramine, 200 nM labetalol and 2 μM ketoprofen). Samples were centrifuged at 3,220 g for 40 minutes. 90 μL of the supernatant were mixed with 90 μL of ultra-pure H_2O and then used for LC-MS/MS analysis. Peak areas were determined from extracted ion chromatograms.

Protein purification.: *LRH-1 LBD*. BL21(pLysS) *E. coli* were transformed with LRH-1 LBD (residues 299–541) in the pMSC7 vector. Cultures were grown at 37 °C in liquid broth (LB) to an OD_{600} of 0.6 prior to induction of protein expression with 1 mM isopropyl-1-thio-D-galactopyranoside (IPTG). Cultures were grown for 4 hours at 30 °C following induction. Cells were harvested by centrifugation and resuspended into lysis buffer containing 20 mM Tris (pH 7.5), 150 mM NaCl, 5% glycerol, and 0.1 mM phenylmethylsulphoyl fluoride (PMSF). Protein was purified by nickel affinity chromatography with Buffer A of 20 mM Tris HCl (pH 7.4), 150 mM NaCl, 5% glycerol, and 25 mM imidazole and Buffer B of 150 mM Tris HCl (Buffer A containing 500 mM imidazole). Protein was incubated with DLPC (4-fold molar excess) overnight at 4 °C to displace copurifying *E. coli* PL. The protein was then re-purified by size exclusion into assay buffer (20 mM Tris HCl (pH 7.4), 150 mM NaCl, 5% glycerol), concentrated to ~3 mg/ ml, and stored at −80 °C. The same purification strategy was used for protein containing the point mutations described in the text.

Full-length LRH-1 (FL-LRH-1).: FL-LRH-1 (residues 1–495, isoform 1, codon optimized for *E. coli*) was cloned into a PET28b vector with a His-SUMO tag and transformed into BL21 (DE3) *E. coli* cells. Cells were grown in LB media at 37 °C to an OD_{600} of 0.5. Protein expression was induced with 0.2 mM IPTG and grown overnight at 16 °C. Cells were harvested by centrifugation and resuspended into lysis buffer containing 20 mM Tris (pH 7.5), 500 mM NaCl, 5% glycerol, 25 mM imidazole, 0.5 mM *tris*(2-carboxyethyl) phosphine (TCEP), and 0.1 mM PMSF. Cells were lysed by sonication for 8 minutes and clarified by centrifugation. Protein was purified by nickel affinity chromatography with elution buffer of 20 mM Tris HCl (pH 7.5), 500 mM NaCl, 5% glycerol, 0.5 mM TCEP and 125 mM imidazole. Ion-exchange chromatography was used to remove DNA with tandem Hitrap Q-SP columns (GE Healthcare). Protein was flowed through the Q column onto the SP column, from which it eluted as a single peak using a linear gradient of NaCl from 0.35 M to 1 M. Finally, the protein was purified to homogeneity by size exclusion chromatography. Functionality of the purified protein was determined by testing its ability to bind DNA containing an LRH-1 response element, and its ability to bind ligand. DNA binding was measured using fluorescence polarization with a 6-carboxyfluorescein (cFAM)-labeled double-stranded DNA probe containing the LRH-1 binding element from the CYP7A1 promoter. FL-LRH-1 was titrated against 10 nM

FAM-CYP7A1 in buffer containing 20 mM Tris (pH 7.5), 150 mM NaCl, 5% glycerol and 0.5 mM TCEP, with a final volume of 50 μl, and incubated at room temperature for 30 min. Polarization was monitored on a Synergy 4 microplate reader (Biotek) at excitation/emission wavelengths of 485/528 nm. Curves were fit using a one-site specific binding equation with baseline-subtraction of wells containing protein but no probe. One biological replicate was conducted with two technical replicates. Ligand binding ability was verified by fluorescence polarization as described below.

Generation of apo LRH-1.—To extract lipids from LRH-1 LBD, 1 ml of purified protein (3 mg) was added to 3.75 ml of chloroform-methanol solution (1:2 v/v) and vortexed briefly. An additional 2.5 ml chloroform:water solution (1:1 v/v) was added and the mixture was vortexed again. The stripped and unfolded protein was pelleted by centrifugation at 1000 rpm for 10 minutes. The resulting protein pellet was dissolved into 0.5 ml of buffer containing 50 mM Tris (pH 8.0), 6 M guanidine hydrochloride and 2 mM DTT. Protein was refolded by fast dilution at 4 °C into 20 mM Tris (pH 8.5), 1.7 M urea, 4% glycerol and 2 mM DTT (25 ml). The final urea concentration was adjusted to 2 M, and the protein was concentrated to ~ 1.5 ml, followed by overnight dialysis against PBS containing 2 mM DTT at 4 °C. Refolded protein was purified by size exclusion chromatography to remove aggregates and remaining unfolded protein. Ligand binding ability was verified by fluorescence polarization as described below.

Mutagenesis.—Mutations were introduced to LRH-1 in the pMSC7 and pCI vectors using the Quikchange Lightning Site-Directed Mutagenesis Kit as directed by the manufacturer (Agilent). Constructs were sequenced prior to use.

Ligand binding assay.—Assays were conducted in black, polystyrene, non-binding surface 384-well plates (Corning) with 30 μl volumes in assay buffer (150 mM NaCl, 20 mM Tris-HCl pH 7.4, 5% glycerol). Plates were incubated overnight at 4 °C and centrifuged briefly before polarization measurement. Polarization was monitored on a Neo plate reader (Biotek) at excitation/emission wavelengths of 485/528 nm. To determine reaction conditions, we first measured the binding affinity of the fluorescein amidite (FAM)-labeled probe (6N-FAM) for WT and mutant LRH-1 by titrating the purified protein in the presence of 10 nM 6N-FAM, as previously described.(D'Agostino et al., 2020) The affinity and B_{max} of 6N-FAM for WT and mutant LRH-1 LBD were used to determine probe and protein concentrations for competition experiments: 10 nM 6N-FAM plus 5, 10, and 15 nM WT, K520A, or Y516A LRH-1, respectively). These assay conditions were validated using unlabeled 6N ligand, which completely outcompeted the probe for both mutant and WT LRH-1. Competition experiments used unlabeled agonists at a concentration range of 200 pM-200 M. Experiments were conducted twice in quadruplicate, and compiled data was fit to a one-site, fit K_i curve. Statistical significance between K_i values was determined by two-way ANOVA followed by Dunnett's test for multiple comparisons. For visual comparison of curves from WT or mutant protein (Figure S7), we normalized the data to competition curves generated from unlabeled 6N. To do this, FP data were baseline-subtracted, using the FP measurement from wells with the lowest concentration of competitor as the baseline. Then, we calculated the percent probe displacement at each concentration point relative to

probe displacement by unlabeled 6N. This did not change the K_i, but it put the curves on the same scale for better visual representation.

Crystallography.—LRH-1 LBD was purified by nickel affinity chromatography as described above. The His tag was cleaved overnight at 4 °C using tobacco etch virus (TEV) protease with dialysis against buffer containing 150 mM NaCl, 5% glycerol, and 20 mM Tris HCl (pH 7.4). Because untagged LRH-1 maintains some affinity for the nickel column, we separated cleaved protein was separated from the cut tag and His-tagged TEV by using 60 mM imidazole to elute LRH-1, and 500 mM imidazole to elute the tag and TEV. Purified protein was incubated overnight at 4 °C with 4–5-fold molar excess of ligand, repurified by size exclusion chromatography into crystallization buffer (150 mM NaCl, 100 mM ammonium acetate (pH 7.4), 1 mM DTT, and 1 mM EDTA, 2 mM 3-[(3-cholamidopropyl)dimethylammonio]-1propanesulfonic acid (CHAPS)), and then incubated with 4-fold molar excess of Tif2 peptide (H_3N-KENALLRYLLDK-CO_2^-) for two hours at room temperature. Crystallization conditions for each complex were as follows:

> *LRH-1–10CA-Tif2:* The LRH-1-10CA-TIF2 complex was concentrated to 5 mg/mL. Crystals were generated at room temperature in 0.4 M N/K tartrate in 96-well sitting drop plates.

> *LRH-1–9ChoP-Tif2:* Crystals were generated by soaking 9ChoP into LRH-1–10CA-Tif2 crystals. First, we generated LRH-1–10CA-Tif2 crystals in larger drops by microseeding, using LRH-1–10CA-Tif2 crystals described above as seed stocks. Fresh LRH-1–10CA-Tif2 complex was concentrated to 5.2 mg/mL, and the seed stock was added to the protein at a dilution of 1:100. The complex was then crystallized by sitting drop vapor diffusion at 4 °C, in drops containing 1 μl protein/ seed stock plus 2 μl 9–19% tert-butanol, 0–6 % glycerol, 0.1 M tri-sodium citrate pH 4.6. 9ChoP was soaked into the crystal drops at 1 μM (~1% DMSO) for two days, and 1 μM 9ChoP was also added to the cryoprotectant.

Structure Determination.—Crystals were flash-frozen in liquid nitrogen using a cryoprotectant of 30% glycerol in crystallant. Data were collected remotely from Argonne National Laboratory (South East Regional Collaborative Access Team, 22ID beamline). Data were processed and scaled using HKL2000 (Otwinowski, 1997) and phased by molecular replacement using Phaser-MR in Phenix (Adams et al., 2010) with PDB 5L11 as the search model. For the 9ChoP structure, the 10CA structure was used as the search model. Coot (Emsley and Cowtan, 2004) and Phenix.refine (Adams et al., 2010) were used for model building and refinement, respectively. Figures were constructed using Pymol (Schrodinger, 2010). Measurements to determine displacement of helix 10 were between C-alphas of residue N523 for each protein.

Hydrogen-deuterium exchange mass spectrometry (HDX-MS).—Following affinity purification and removal of the His-tag as described above, LRH-1 LBD protein was re-purified by size exclusion chromatography into an assay buffer of phosphate-buffered saline, pH 7.5, plus 5% glycerol. Protein aliquots (2 mg/ml) were incubated with carboxylic acid derivatives 4CA, 5CA, 9CA, or 10CA at 5-fold molar excess, overnight at 4 °C.

Samples were diluted 1:7 (v/v) in labeling buffer to initialize exchange reactions (same as the protein buffer but containing 99.9 % D_2O instead of H_2O). The reactions were quenched after 0, 10, 100, 1000 and 10000 seconds by adding equal volume of precooled quenching buffer (100 mM phosphate, 0.5 M tris(2-carboxyethyl) phosphine, 0.8% formic acid, and 2% acetonitrile, pH 2.5). Reactions for each sample at each time point were performed in triplicate. Quenched samples were passed through an Enzymate BEH pepsin column (Waters). Fragmented peptides were separated by an C18 UPLC column and analyzed by a Q-Tof Premier mass spectrometer. ProteinLynx Global SERVER™ (PLGS) was used to identify peptides by database searching of LRH-1 LBD sequence. The HDX-MS data were further processed using DynamX (v3.0) and the differential HDX between ligand-bound states was calculated by comparing the relative fractional uptake for each residue at given time.

NR-coregulator recruitment by MARCoNI.—Assay mixes consisted of 25 nM ALEXA488-conjugated penta-His antibody (Qiagen # 35310), 50 μM DTT, 20mM Tris (pH 7.4), 250mM NaCl, 0.5 mM TCEP and purified protein: either (1) 50 nM His-LRH-1 LBD (in the apo state or pre-loaded with compounds), or (2) 50 nM His-SUMO-hLRH-1-FL (bound to copurifying PL from *E. coli* or preloaded with compound during purification). Compounds (dissolved in DMSO) were added to the assay mixes at final concentrations of 10 μM. DMSO was 2% v/v in all mixes. Coregulator profiling was conducted by Microarray Assay for Real-time Coregulator Nuclear Receptor Interaction (MARCoNI), using PamChip #88101.(Aarts et al., 2013) LRH-1-coregulator binding was measured in triplicate and quantified using BioNavigator software (PamGene). The compound-induced log-fold change (LFC) of LRH-1 binding to each coregulator peptide and statistical significance (FDR threshold of 0.05 and Student's t-test) were calculated and visualized using R software (R Core Team, 2017). Compound and interaction (dis)similarity were calculated by Hierarchical Clustering on Euclidean Distance and Ward's agglomeration. Upset plots were generated using the R package UpSetR v1.4.0 (Conway et al., 2017).

Molecular dynamics simulations.—Two crystal structures of LRH-1 LBD in complex with Tif2 were used for model construction (1) PDB 7JYD (10CA ligand) and (2) PDB 4DOS (DLPC). Structures were modified at the N and C termini so that they included residues 300–540 of LRH-1 and residues 742–751 of Tif2. Missing residues and sidechains within this protein sequence were added. All complexes were solvated in an octahedral box of TIP3P water with a 10 Å buffer around the complex. Na^+ and Cl^-ions were added to neutralize the complex and achieve physiological conditions (150 mM sodium chloride). All systems were generated with the Xleap module of AmberTools(Case et al., 2017), using the ff14SB force field.(Maier, 2015) Parameters for all ligands were obtained using the Antechamber module(Wang, 2001) of AmberTools. All minimizations and simulations were performed with Amber17 (Case et al., 2017). Using a minimization protocol of 5000 steps of steepest descent followed by 5000 steps of conjugate gradient, systems were minimized in an iterative manner: i) with 500 kcal/mol.$Å^2$restraints on all atoms; ii) with 500 kcal/mol.$Å^2$ restraints on restraints retained on ligand and peptide atoms; iii) with restraints removed from all atoms. Following minimization, systems were heated from 0 to 300 K using a 100-ps run with constant volume periodic boundaries and 5 kcal/mol.$Å^2$ restraints

on all protein and ligand atoms. Equilibration was performed using a 12-ns MD run with 10 kcal/mol.Å^2 restraints on protein and ligand atoms using the NPT ensemble. Restraints were reduced to 1 kcal/mol.Å^2 for an additional 10 ns of equilibration. All restraints were removed, and production runs were performed for 1 μs in the NPT ensemble. A 2-fs time step was used for all simulations. All bonds between heavy atoms and hydrogens were fixed with the SHAKE algorithm.(Ryckaert, 1977) A 10-Å cutoff was used for nonbonded interactions. Long range electrostatics were evaluated using Particle Mesh Ewald (PME). For analysis, frames were obtained at 20 ps intervals from each simulation. The CPPTRAJ module (Roe and Cheatham III, 2013) of AmberTools was used for structural averaging of MD trajectories and distance calculations. The stability of hydrogen bonds between ligands and protein was calculated by measuring the distances between heavy atoms of interacting residues (for example, C of carboxylate groups, N of amino groups, O of hydroxyl groups) over the course of the simulations and quantifying the percentage of time they were within 3.5 Å of each other.

Agonist treatment of Huh7 cells.—Huh7 cells were plated in 6-well plates at 5×10^5 cells/well. After 24 hours, cells were treated with vehicle (0.1% DMSO in media) or indicated concentrations of 10CA. Cells were collected for RNA extraction after 24 hours of treatment. RNA extraction was performed using the RNAeasy Mini RNA extraction kit (Qiagen).

Viral overexpression and drug treatment in mice.—Adeno-associated virus serotype 8 (AAV8) expressing N-terminal Avi-tagged human LRH-1 and AAV8-GFP (used as a negative control) were obtained from Vector Biolabs (Malvern, PA, USA). C57BL/6J mice were administered 1×10^{12} genome copies (GC)/mL via femoral vein injection. Two weeks after virus treatment, mice (n = 5) were administered 0.1, 1.0, or 10 mg/ kg of 10CA or vehicle (5% ethanol in corn oil) via intraperitoneal injection five times over a 3-day period. Mice were treated each morning and evening for two days and on the morning of day 3. Mice were euthanized on day 3, approximately four hours after the final drug treatment. Mouse liver tissue was collected, flash-frozen in liquid nitrogen, and stored at −80 °C. RNA was extracted from the liver samples using the miRNAeasy Mini kit (Qiagen), following cryo-pulverization of the tissues in liquid nitrogen and homogenization in Trizol (Invitrogen). A portion of the RNA was retained for NanoString analysis, and a portion was subjected to qRT-PCR to verify overexpression of hLRH-1. Reverse transcription was performed using the High Capacity cDNA Reverse Transcription Kit (Applied Biosystems). qRT-PCR used the *Power* SYBR™ Green PCR Master Mix (Applied Biosystems) and run on a StepOnePlus™ Real-Time PCR instrument (Applied Biosystems). Data were analyzed via the C_t method, with *Tata binding protein* (*Tbp*) as the reference gene. Primer sequences are shown in Table S2.

NanoString Gene Expression Analysis.—RNA concentrations were measured on a Nanodrop 1000, and quality was assessed on a 2100 Bioanalyzer Instrument (Agilent) using the RNA 6000 Nano (25ng/μl – 1,000ng/μl) or Pico assay (0.5ng/ul – 20ng/μl). All RNA Integrity (RIN) scores were >9.0. 25ng of total RNA was hybridized with biotin-labeled capture probes and fluorescently-labeled reporter probes (NanoString Technologies, Inc.)

for 18 hours at 65 °C. Following hybridization, samples were injected into a NanoString SPRINT cartridge and loaded onto the nCounter SPRINT Profiler instrument, where hybridized mRNAs were immobilized for imaging and excess probes were removed. Following image acquisition, mRNA counts were extracted from raw RCC files using nSolver™ data analysis software (v4.0, NanoString Technologies, Inc.). Significance was assessed by two-way ANOVA, followed by Benjamini-Yekutieli False Discovery Rate (FDR) method using an FDR threshold of 0.05, as recommended by Nanostring gene expression guidelines. Hierarchical clustering of the data on Euclidean distance and Ward's agglomeration was done using the R package ComplexHeatmap (Gu et al., 2016).

Humanized LRH-1 Mouse Intestinal Enteroid Culture.—Intestinal crypt cultures (enteroids) were derived from LRH-1 KO (LRH-1$^{f/f}$;Villin-Cre+), and hLRH-1 (LRH-1$^{f/f}$;hLRH-1 ;Villin-Cre+) male mice (6−8 weeks old)(Bayrer et al., 2018). Briefly, the small intestine was isolated and flushed with ice-cold PBS, opened longitudinally, then cut into 1−2 mm pieces. Intestinal fragments were incubated in an EDTA-containing solution (4 mM) at 4 °C for 60 min on a tube rocker. The intestinal fragment suspension was fractionated by vertical shaking manually and crypt-containing fractions passed through a 70 μm cell strainer for plating in Matrigel. The crypt-Matrigel suspension was allowed to polymerize at 37 °C for 15 min. Intestinal organoids were grown in base culture media (Advanced DMEM/F12 media, HEPES, GlutaMax, penicillin, and streptomycin) supplemented with growth factors (EGF, Noggin, R-spondin, R&D Systems), B27 (Life Technologies), N2 (Life Technologies), and N-acetyl cysteine (Sigma). Intestinal enteroids were passaged every 3 days. Established hLRH-1 or LRH-1 KO enteroids were treated with mouse TNF-α overnight to provoke inflammatory changes, then treated with vehicle (DMSO) or compound 10CA (1 μM) overnight. Following the treatment, enteroid tissues were harvested for real-time PCR.

RNA Isolation and qRT-PCR of enteroids.—Enteroids were washed in ice cold PBS and suspended in Trizol solution (Sigma). RNA was isolated with RNeasy spin columns (Qiagen). DNase-treated total RNA was used to generate cDNA using Superscript II (Quanta). SYBR green-based qPCR (Kapa Biosystems) was performed on a Roche LightCycler 480 II. The C_t method was used for calculating gene expression fold changes using Rplp0 (ribosomal protein, large, P0, known as 36B4) as the reference. Primer sequences are shown in Table S2.

T Cell transfer model of colitis.—For T cell transfer experiments, $hLRH1^{IEC}$ mice were used to induce the chronic enterocolitis as described(Ostanin et al., 2009). Briefly, wild-type splenic $CD4^+CD45RB^{high}$ cells were isolated by MACS separation and flow cytometry cell sorting, and then transferred by intraperitoneal injection to recipient mice (0.5×10^6 cells/mice). All recipients were weighed immediately prior to T cell transfer to determine baseline weight, and then weighed twice weekly after T cell transfers for the duration of the experiment. 10CA treatment started from week 4 after the T cell transfer, 20 mg/kg 10CA in sterile saline was injected intraperitoneally (i.p.) 6 days per week. Normal saline was used as control treatment. Transferred recipient mice were euthanized upon losing 20% of

pre-transfer baseline weight. All recipient mice receiving different treatment were co-housed throughout to normalize microflora exposure.

At the end of treatment, disease activity scores were assessed according to Table S3. For colon histological analysis, the colon was divided into three segments (proximal, middle, and distal). Each segment was embedded in paraffin, sectioned at 5 μm, and stained with hematoxylin and eosin. Histological analysis was performed in the Cellular and Molecular Morphology Core of the Digestive Disease Center at Baylor College of Medicine. The sections were blindly scored using a standard histologic colitis score. Three independent parameters were measured: severity of inflammation (0–3: none, slight, moderate, severe), depth of injury (0–3: none, mucosal, mucosal and submucosal, transmural), and crypt damage (0–4: none, basal one-third damaged, basal two-thirds damaged, only surface epithelium intact, entire crypt and epithelium lost). The score of each parameter was multiplied by a factor reflecting the percentage of tissue involvement ($\times 1$, 0–25%; $\times 2$, 26–50%; $\times 3$, 51–75%; $\times 4$, 76–100%) averaged per colon.

QUANTIFICATION AND STATISTICAL ANALYSIS

All statistical analyses were conducted using GraphPad Prism, v9. The statistical tests used and alpha level considered to be significant for each comparison are reported in the figure legends.

Supplementary Material

Refer to Web version on PubMed Central for supplementary material.

Acknowledgements

Inclusion and Diversity

One or more of the authors of this paper received support from a program designed to increase minority representation in science. One or more of the authors of this paper self-identifies as living with a disability.

Abbreviations

PL	phospholipid
PC	phosphatidylcholine
DLPC	dilauroylphosphatidylcholine

LRH-1	liver receptor homolog-1
NR	nuclear hormone receptor
ChoP	phosphorylcholine
CA	carboxylic acid
Tif2	transcriptional intermediary factor 2
6HP	hexahydropentalene
HDX-MS	hydrogen-deuterium exchange mass spectrometry
AFS	activation function surface
AF-H	activation function helix
MARCoNI	Microarray Assay for Real-time Coregulator-Nuclear Receptor Interactions
TCT	T-cell transfer

References

Aarts JM, Wang S, Houtman R, van Beuningen RM, Westerink WM, Van De Waart BJ, Rietjens IM, and Bovee TF (2013). Robust array-based coregulator binding assay predicting ERalpha-agonist potency and generating binding profiles reflecting ligand structure. Chem Res Toxicol 26, 336–346. [PubMed: 23383871]

Adams PD, Afonine PV, Bunkoczi G, Chen VB, Davis IW, Echols N, Headd JJ, Hung LW, Kapral GJ, Grosse-Kunstleve RW, et al. (2010). PHENIX: a comprehensive Python-based system for macromolecular structure solution. Acta Crystallogr D Biol Crystallogr 66, 213–221. [PubMed: 20124702]

Basak O, Beumer J, Wiebrands K, Seno H, van Oudenaarden A, and Clevers H (2017). Induced Quiescence of Lgr5+ Stem Cells in Intestinal Organoids Enables Differentiation of Hormone-Producing Enteroendocrine Cells. Cell Stem Cell 20, 177–190 e174. [PubMed: 27939219]

Bayrer JR, Wang H, Nattiv R, Suzawa M, Escusa HS, Fletterick RJ, Klein OD, Moore DD, and Ingraham HA (2018). LRH-1 mitigates intestinal inflammatory disease by maintaining epithelial homeostasis and cell survival. Nat Commun 9, 4055. [PubMed: 30305617]

Bouguen G, Langlois A, Djouina M, Branche J, Koriche D, Dewaeles E, Mongy A, Auwerx J, Colombel JF, Desreumaux P, et al. (2015). Intestinal steroidogenesis controls PPARgamma expression in the colon and is impaired during ulcerative colitis. Gut 64, 901–910. [PubMed: 25053717]

Case D, Cerutti DS, Cheatham TE III, Darden T, Duke R, Giese T, Gohlke H, Goetz A, Greene D, Homeyer N, et al. (2017). AMBER 2017. University of Californa, San Franscisco.

Chakravarthy MV, Lodhi IJ, Yin L, Malapaka RR, Xu HE, Turk J, and Semenkovich CF (2009). Identification of a physiologically relevant endogenous ligand for PPARalpha in liver. Cell 138, 476–488. [PubMed: 19646743]

Chaurio RA, Janko C, Munoz LE, Frey B, Herrmann M, and Gaipl US (2009). Phospholipids: key players in apoptosis and immune regulation. Molecules 14, 4892–4914. [PubMed: 20032867]

Chen M, Pan H, Dai Y, Zhang J, Tong Y, Huang Y, Wang M, and Huang H (2017). Phosphatidylcholine regulates NF-κB activation in attenuation of LPS-induced inflammation: evidence from in vitro study. Animal Cells and Systems 22, 7–14.

Choi S, Dong B, Lin CJ, Heo MJ, Kim KH, Sun Z, Wagner M, Suh JM, Wang MC, and Moore DD (2019). Methyl-sensing nuclear receptor Liver Receptor Homolog-1 regulates mitochondrial function in mouse hepatocytes. Hepatology 71, 1055–1069. [PubMed: 31355949]

Cobo-Vuilleumier N, Lorenzo PI, Rodriguez NG, Herrera Gomez IG, Fuente-Martin E, Lopez-Noriega L, Mellado-Gil JM, Romero-Zerbo SY, Baquie M, Lachaud CC, et al. (2018). LRH-1 agonism favours an immune-islet dialogue which protects against diabetes mellitus. Nat Commun 9, 1488. [PubMed: 29662071]

Conway JR, Lex A, and Gehlenborg N (2017). UpSetR: an R package for the visualization of intersecting sets and their properties. Bioinformatics 33, 2938–2940. [PubMed: 28645171]

Cornelison JL, Cato ML, Johnson AM, D'Agostino EH, Melchers D, Patel AB, Mays SG, Houtman R, Ortlund EA, and Jui NT (2020). Development of a new class of liver receptor homolog-1 (LRH-1) agonists by photoredox conjugate addition. Bioorganic & Medicinal Chemistry Letters 30, 1–18.

Coste A, Dubuquoy L, Barnouin R, Annicotte J-S, Magnier B, Notti M, Corazza N, Antal MC, Metzger D, Desreumaux P, et al. (2007). LRH-1-mediated glucocorticoid synthesis in enterocytes protects against inflammatory bowel disease. Proc Natl Acad Sci U S A 104, 13098–13103. [PubMed: 17670946]

D'Agostino EH, Flynn AR, Cornelison JL, Mays SG, Patel A, Jui NT, and Ortlund EA (2020). Development of a Versatile and Sensitive Direct Ligand Binding Assay for Human NR5A Nuclear Receptors. ACS Med Chem Lett 11, 365–370. [PubMed: 32184971]

Dawaliby R, Trubbia C, Delporte C, Masureel M, Van Antwerpen P, Kobilka BK, and Govaerts C (2016). Allosteric regulation of G protein-coupled receptor activity by phospholipids. Nat Chem Biol 12, 35–39. [PubMed: 26571351]

Emsley P, and Cowtan K (2004). Coot: model-building tools for molecular graphics. Acta Crystallogr D Biol Crystallogr 60, 2126–2132. [PubMed: 15572765]

Fernandez-Marcos PJ, Auwerx J, and Schoonjans K (2011). Emerging actions of the nuclear receptor LRH-1 in the gut. Biochim Biophys Acta 1812, 947–955. [PubMed: 21194563]

Flynn AR, Mays SG, Ortlund EA, and Jui NT (2018). Development of Hybrid Phospholipid Mimics as Effective Agonists for Liver Receptor Homologue-1. ACS Med Chem Lett 9, 1051–1056. [PubMed: 30344916]

Furse S, and de Kroon AI (2015). Phosphatidylcholine's functions beyond that of a membrane brick. Mol Membr Biol 32, 117–119. [PubMed: 26306852]

Geiss GK, Bumgarner RE, Birditt B, Dahl T, Dowidar N, Dunaway DL, Fell HP, Ferree S, George RD, Grogan T, et al. (2008). Direct multiplexed measurement of gene expression with color-coded probe pairs. Nature Biotechnology 26, 317–325.

Gensler LS (2013). Glucocorticoids: complications to anticipate and prevent. Neurohospitalist 3, 92–97. [PubMed: 23983891]

Gu Z, Eils R, and Schlesner M (2016). Complex heatmaps reveal patterns and correlations in multidimensional genomic data. Bioinformatics 32, 2847–2849. [PubMed: 27207943]

Koppen A, Houtman R, Pijenburg D, Jeninga EH, Ruijtenbeek R, and Kalkhoven E (2009). Nuclear Receptor-Coregulator Interaction Profiling Identifies TRIP3 as a Novel Peroxisome Proliferator-activated Receptor. Molecular and Cellular Proteomics, 2211–2226.

Lee JM, Lee YK, Mamrosh JL, Busby SA, Griffin PR, Pathak MC, Ortlund EA, and Moore DD (2011). A nuclear-receptor-dependent phosphatidylcholine pathway with antidiabetic effects. Nature 474, 506–510. [PubMed: 21614002]

Li Z, Agellon LB, Allen TM, Umeda M, Jewell L, Mason A, and Vance DE (2006). The ratio of phosphatidylcholine to phosphatidylethanolamine influences membrane integrity and steatohepatitis. Cell Metab 3, 321–331. [PubMed: 16679290]

Lin CJ, and Wang MC (2017). Microbial metabolites regulate host lipid metabolism through NR5A-Hedgehog signalling. Nat Cell Biol 19, 550–557. [PubMed: 28436966]

Liu S, Brown JD, Stanya KJ, Homan E, Leidl M, Inouye K, Bhargava P, Gangl MR, Dai L, Hatano B, et al. (2013). A diurnal serum lipid integrates hepatic lipogenesis and peripheral fatty acid use. Nature 502, 550–554. [PubMed: 24153306]

Lu T, Makishima M, JJ R, Schoonjans K, Kerr T, Auwerx J, and DJ M (2000). Molecular Basis for Feedback Regulation of Bile Acid Synthesis by Nuclear Receptors. Mol Cell 6, 507–515. [PubMed: 11030331]

MacDonald JI, Specher H (1991). Phospholipid Fatty Acid Remodeling in Mammalian Cells. Biochim Biophys Acta, Lipids Lipid Metab 1084, 105–121.

Maier JAM, C.; Kasavajhala K; Wickstrom L; Hauser KE; Simmerling C (2015). ff14SB: Improving the accuracy of protein side chain and backbone parameters from ff99SB. Journal of chemical theory and computation 11, 3696–3713.

Mamrosh JL, Lee JM, Wagner M, Stambrook PJ, Whitby RJ, Sifers RN, Wu SP, Tsai MJ, Demayo FJ, and Moore DD (2014). Nuclear receptor LRH-1/NR5A2 is required and targetable for liver endoplasmic reticulum stress resolution. eLife 3, e01694. [PubMed: 24737860]

Mays SG, Flynn AR, Cornelison JL, Okafor CD, Wang H, Wang G, Huang X, Donaldson HN, Millings EJ, Polavarapu R, et al. (2019). Development of the first low nanomolar liver receptor homolog-1 agonist through structure-guided design. J Med Chem 62, 11022–11034. [PubMed: 31419141]

Mays SG, Okafor CD, Tuntland ML, Whitby RJ, Dharmarajan V, Stec J, Griffin PR, and Ortlund EA (2017). Structure and Dynamics of the Liver Receptor Homolog 1-PGC1alpha Complex. Mol Pharmacol 92, 1–11. [PubMed: 28363985]

Mays SG, Okafor CD, Whitby RJ, Goswami D, Stec J, Flynn AR, Dugan MC, Jui NT, Griffin PR, and Ortlund EA (2016). Crystal Structures of the Nuclear Receptor, Liver Receptor Homolog 1, Bound to Synthetic Agonists. J Biol Chem 291, 25281–25291. [PubMed: 27694446]

Mueller M, Cima I, Noti M, Fuhrer A, Jakob S, Dubuquoy L, Schoonjans K, and Brunner T (2006). The nuclear receptor LRH-1 critically regulates extra-adrenal glucocorticoid synthesis in the intestine. J Exp Med 203, 2057–2062. [PubMed: 16923850]

Musille PM, Kohn JA, and Ortlund EA (2013a). Phospholipid - Driven gene regulation. FEBS Letters 587, 1238–1246. [PubMed: 23333623]

Musille PM, Kossmann BR, Kohn JA, Ivanov I, and Ortlund EA (2015). Unexpected Allosteric Network Contributes to LRH-1 Coregulator Selectivity. J Biol Chem 291, 1411–1426. [PubMed: 26553876]

Musille PM, Pathak M, Lauer JL, Griffin PR, and Ortlund EA (2013b). Divergent sequence tunes ligand sensitivity in phospholipid-regulated hormone receptors. J Biol Chem 288, 20702–20712. [PubMed: 23737522]

Musille PM, Pathak MC, Lauer JL, Hudson WH, Griffin PR, and Ortlund EA (2012). Antidiabetic phospholipid-nuclear receptor complex reveals the mechanism for phospholipid-driven gene regulation. Nat Struct Mol Biol 19, 532–537, S531–532. [PubMed: 22504882]

Na S-Y, Kim H-J, Lee S-K, Choi H-S, Na D-S, Lee M-O, Chung M, Moore DD, and Lee JW (1998). IkBb Interacts with the Retinoid X Receptor and Inhibits Retinoid-dependent Transactivation in Lipopolysaccharide-treated Cells. J Biol Chem 273, 3212–3215. [PubMed: 9452433]

Nadolny C, and Dong X (2015). Liver receptor homolog-1 (LRH-1): a potential therapeutic target for cancer. Cancer Biol Ther 16, 997–1004. [PubMed: 25951367]

Olson A, Diebel LN, and Liberati DM (2014). Exogenous phosphatidylcholine supplementation improves intestinal barrier defense against Clostridium difficile toxin. J Trauma Acute Care Surg 77, 570–575; discussion 576. [PubMed: 25250596]

Ordás I, Eckmann L, Talamini M, Baumgart DC, and Sandborn WJ (2012). Ulcerative colitis. The Lancet 380, 1606–1619.

Ortlund EA, Lee Y, Solomon IH, Hager JM, Safi R, Choi Y, Guan Z, Tripathy A, Raetz CR, McDonnell DP, et al. (2005). Modulation of human nuclear receptor LRH-1 activity by phospholipids and SHP. Nat Struct Mol Biol 12, 357–363. [PubMed: 15723037]

Ostanin DV, Bao J, Koboziev I, Gray L, Robinson-Jackson SA, Kosloski-Davidson M, Price VH, and Grisham MB (2009). T cell transfer model of chronic colitis: concepts, considerations, and tricks of the trade. Am J Physiol Gastrointest Liver Physiol 296, G135–146. [PubMed: 19033538]

Otwinowski Z, Minor W (1997). Processing of X-Ray Diffraction Data Collected in Oscillation Mode. Method Enzymol 276, 307–326.

Roe DR, and Cheatham TE III (2013). PTRAJ and CPPTRAJ: software for processing and analysis of molecular dynamics trajectory data. Journal of chemical theory and computation 9, 3084–3095. [PubMed: 26583988]

Ryckaert J-PC, G.; Berendsen HJ (1977). Numerical integration of the cartesian equations of motion of a system with constraints: molecular dynamics of n-alkanes. Journal of Computational Physics 23, 327–341.

Sablin EP, Blind RD, Uthayaruban R, Chiu HJ, Deacon AM, Das D, Ingraham HA, and Fletterick RJ (2015). Structure of Liver Receptor Homolog-1 (NR5A2) with PIP hormone bound in the ligand binding pocket. J Struct Biol 192, 342–348. [PubMed: 26416531]

Schneider H, Braun A, Fullekrug J, Stremmel W, and Ehehalt R (2010). Lipid based therapy for ulcerative colitis-modulation of intestinal mucus membrane phospholipids as a tool to influence inflammation. Int J Mol Sci 11, 4149–4164. [PubMed: 21152327]

Schrodinger LLC (2010). The PyMOL Molecular Graphics System, Version 1.3r1

Solomon IH, Hager JM, Safi R, McDonnell DP, Redinbo MR, and Ortlund EA (2005). Crystal structure of the human LRH-1 DBD-DNA complex reveals Ftz-F1 domain positioning is required for receptor activity. J Mol Biol 354, 1091–1102. [PubMed: 16289203]

Treede I, Braun A, Sparla R, Kuhnel M, Giese T, Turner JR, Anes E, Kulaksiz H, Fullekrug J, Stremmel W, et al. (2007). Anti-inflammatory effects of phosphatidylcholine. J Biol Chem 282, 27155–27164. [PubMed: 17636253]

van der Veen JN, Kennelly JP, Wan S, Vance JE, Vance DE, and Jacobs RL (2017). The critical role of phosphatidylcholine and phosphatidylethanolamine metabolism in health and disease. Biochim Biophys Acta Biomembr 1859, 1558–1572. [PubMed: 28411170]

Wagner M, Choi S, Panzitt K, Mamrosh JL, Lee JM, Zaufel A, Xiao R, Wooton-Kee R, Stahlman M, Newgard CB, et al. (2016). Liver receptor homolog-1 is a critical determinant of methyl-pool metabolism. Hepatology 63, 95–106. [PubMed: 26267291]

Walker AK (2017). 1-Carbon Cycle Metabolites Methylate Their Way to Fatty Liver. Trends Endocrinol Metab 28, 63–72. [PubMed: 27789099]

Wang JW, W.; Kollman PA; Case DA (2001). Antechamber: an accessory software package for molecular mechanical calculations. J Am Chem Soc 222, U403.

Xu P, Oosterveer MH, Stein S, Demagny H, Ryu D, Moullan N, Comment A, Auwerx J, and Schoonjans K (2016). LRH-1-dependent programming of mitochondrial glutamine processing drives liver cancer. Genes & development 30, 1255–1260. [PubMed: 27298334]

Significance

Phospholipids (PL) can act as ligands for nuclear receptors (NRs), impacting metabolism, growth, and homeostasis via modulating NR transcriptional activity. This paper presents mechanistic and biological evaluation of PL mimetics designed to activate liver receptor homolog-1 (LRH-1), a NR that regulates metabolic homeostasis by binding PL ligands. LRH-1 regulates lipogenesis in the liver, and LRH-1 modulators are highly sought for treatment of metabolic diseases. LRH-1 also controls local inflammation in the gut and barrier function of the intestinal wall, giving it potential as a therapeutic target for inflammatory bowel diseases such as ulcerative colitis (UC). In LRH-1 crystal structures, synthetic agonists bind very differently than PLs, and we hypothesized that incorporating groups that make PL-like contacts would improve activity. Therefore, we designed hybrid molecules by fusing polar groups mimicking PL headgroups to a synthetic LRH-1 agonist. The PL-mimicking group improves affinity and activity of the agonists *in vitro*. It also promotes conformational changes favoring recruitment of a specific complement of coregulator proteins, seen by hydrogen-deuterium exchange mass spectrometry and array-based coregulator recruitment experiments. Crystal structures of LRH-1 bound to two of the PL-mimics demonstrate that they interact as designed and make hydrogen bonds in the targeted part of the pocket. One of the most active PL-mimics *in vitro* also reduces lipogenic gene expression in mouse liver in an LRH-1-dependent manner. It is also active in a murine T-cell transfer model of UC, dramatically reducing intestinal inflammation, intestinal crypt loss, and other markers of disease severity. This *in vivo* evidence of efficacy in UC for a synthetic LRH-1 modulator demonstrates its potential as a therapeutic target for inflammatory bowel diseases.
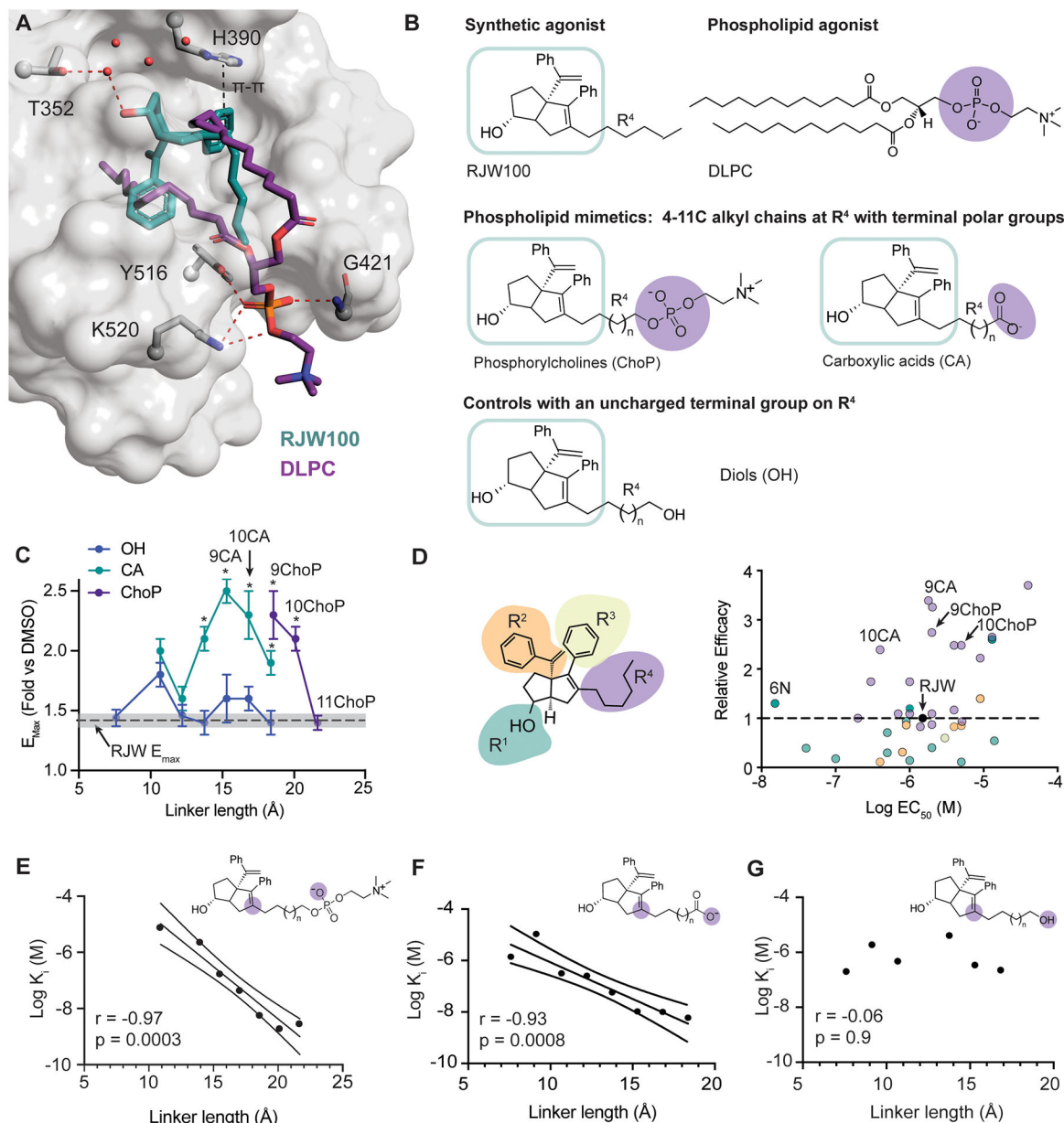
Figure 1. Design, binding, and activity of PL-mimetics.
A. LRH-1 ligand binding pocket (LBP) from PDB 5L11, showing the binding modes
of synthetic agonist RJW100 (teal sticks) and phospholipid agonist DLPC (PDB 4DOS,
purple sticks). Key interactions made by each agonist are highlighted. **B.** *Top*, Chemical
structures of the LRH-1 agonists RJW100 and DLPC. The unmodified portion of RJW100
is highlighted in a teal box, and the PL headgroup of DPLC is highlighted in purple.
These elements were combined to make the PL mimics through modification at position R^4.
Middle, Structures of PL-mimics. ChoP or CA isosteres were conjugated to the RJW100
core via alkyl linkers of 4–11 carbons (Flynn et al., 2018). *Bottom*, Diols with alkyl
linkers of 4–11 carbons were synthesized for comparison with PL mimics. **C.** Plot of
E_{max} values from luciferase reporter assays as a function of linker length. Each point

represents the mean +/− SEM from 2–3 experiments. Compounds that did not activate sufficiently for E_{max} calculation are omitted. *Dotted line* is the mean E_{max} of RJW100; grey shading indicates SEM. *, $p < 0.05$ *versus* RJW100 by two-way ANOVA followed by Sidak's multiple comparisons test. **D.** *Right*, Activity profiles of the PL-mimics *versus* related LRH-1 agonists. *Left*, RJW100 chemical structure, showing the color scheme for the dots in the plot (colored according to the site of modification). Relative efficacy is E_{max} relative to RJW100, calculated as described in Methods. **E-G.** Binding affinity (K_i) plotted as a function of linker length for ChoPs *(E)*, CAs *(F)*, and diols *(G)*. *Lower insets*, Pearson correlation coefficients (r) and p-values. *Upper insets*, illustration of the portion of R^4 used to measure linker length (distance between the two purple spheres).
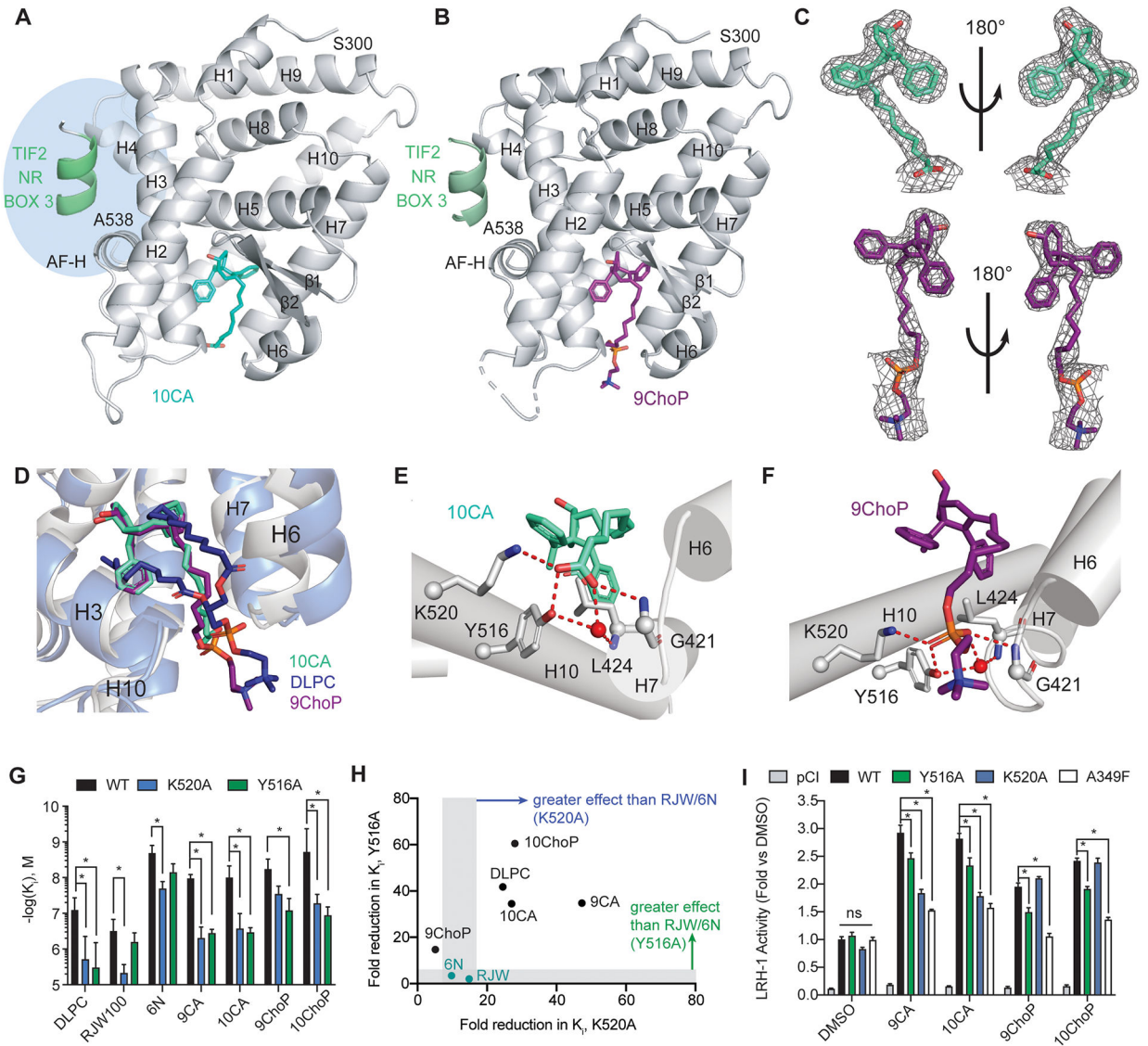
Figure 2. Phospholipid mimetics make PL-like interactions in the LRH-1 binding pocket important for binding and activation.

A-B. Crystal structures of LRH-1 LBD with (**A**) 10CA (PDB: 7JYD) or (**B**) 9ChoP (PDB: 7JYE) and a fragment of the Tif2 coregulator. *H*, helix. In *A*, the AFS (parts of helices 3, 4, and the AF-H) is highlighted in light blue. **C.** Electron density surrounding 10CA (*top*) and 9ChoP (*bottom*). Maps are omit F_o-F_c, contoured at 2 . **D.** Superposition of three ligands from LRH-1 structures: 10CA (cyan sticks), 9ChoP (purple sticks), or DLPC (dark blue sticks, from PBD 4DOS). 10CA and DLPC protein backbones are shown as grey and light blue cartoons, respectively. **E-F.** Close-up of the interactions made by the terminal polar groups of 10CA (*E*) and 9ChoP (*F*). Hydrogen bonds are shown as red dotted lines; water molecule as a red sphere. **G.** Effects of K520A or Y516A mutations on binding affinity. Each bar represents the mean +/− 95% CI from two experiments conducted in quadruplicate. *, $p < 0.05$ by two-way ANOVA followed by Dunnett's test for multiple comparisons. **H.** Fold changes in K_i for mutant *versus* WT LRH-1. Grey shading indicates effects of

the mutations on RJW100 and 6N binding, which do not contact the mutated residues. **I.** Luciferase reporter assays with LRH-1 containing K520A or Y516A mutations. The A349F mutation occludes the pocket and was a negative control. Cells were treated with 30 μM of each compound for 24 hours prior to measurement of luciferase signal. *, $p < 0.05$ *versus* WT LRH-1 treated with each agonist; (two-way ANOVA followed by Dunnett's test for multiple comparisons).
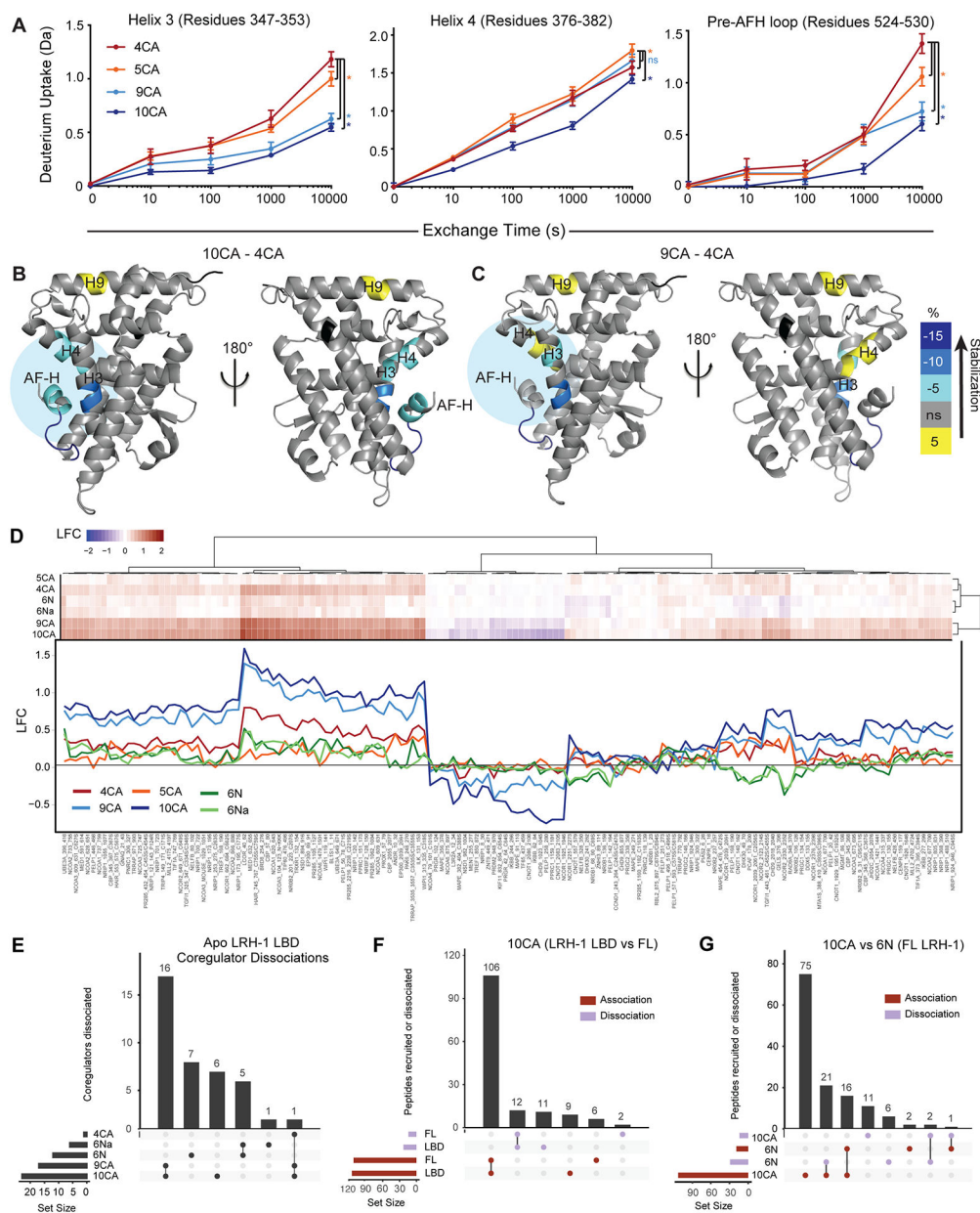
Figure 3. Longer-tailed PL mimetics stabilize the AFS and alter coregulator binding.
A. Plots of deuterium uptake over time from HDX-MS experiments at sites in the LRH-1 AFS. Each point represents the mean +/− SD for three replicates. Slower deuterium exchange indicates greater stability. *, p < 0.05. *versus* 4CA by two-way ANOVA followed by Holm-Sidak's test for multiple comparisons. **B-C.** Differences in deuterium uptake for 10CA-LRH-1 (***B***) and LRH-1–9CA (***C***) *versus* LRH-1–4CA mapped to the structure. *Blue circles*, AFS. *Scale bar* indicates the degree of stabilization (teal and blue) or destabilization (yellow) by 9CA or 10CA. *Black*, unmapped regions. *H*, helix. **D.** Heatmap and corresponding raw traces showing log fold change (LFC) coregulator binding relative to apo-LRH-1-LBD. **E-G.** Upset plots showing overlaps in coregulator binding events affected by at least 1.5-fold. Horizontal bars represent the number of events in each set, and vertical

bars indicate numbers of events that overlap in between the groups that have filled-in circles below them. For example, the first vertical bar in *E* shows that a set of 16 coregulator peptides dissociate from LRH-1 in the presence of 9CA and 10CA that are not affected by 6N and 6Na. **G.** Upset plot comparing overlap in coregulator recruitment events by 10CA bound to full-length LRH-1 (FL) or LRH-1 LBD. Red bars indicate coregulators that associated to the 10CA-LRH-1 complex, and purple bars indicate coregulator dissociation. **H.** Upset plot highlighting an opposite recruitment pattern by compounds 10CA and 6N bound to FL-LRH-1.
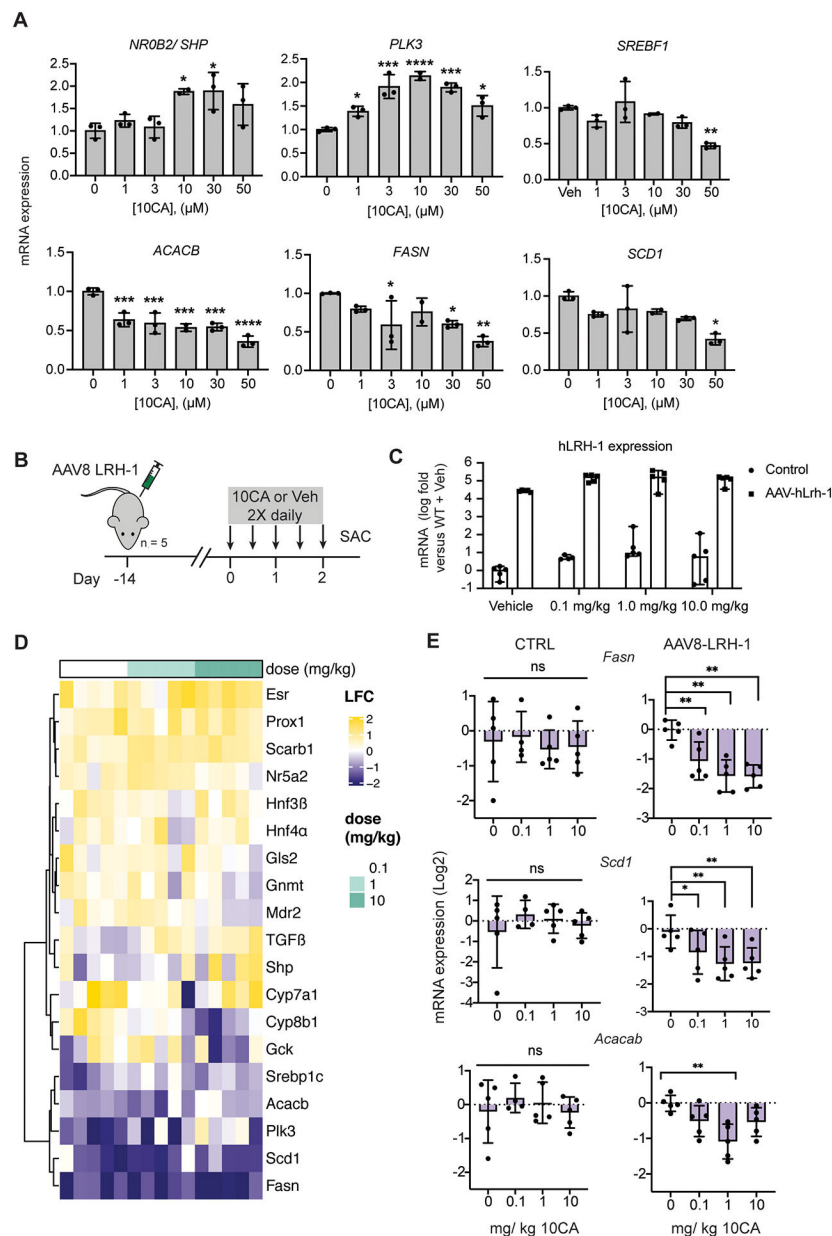
Figure 4. 10CA activates LRH-1 in hepatocytes and in the liver.
A. qRT-PCR analysis of LRH-1 targets in Huh7 hepatocytes. Cells were treated for 24 hours with 10CA concentrations indicated in the x-axes. Each bar represents the mean fold change *versus* DMSO-treated cells, with individual data points shown. Error bars are standard deviation for 2–3 replicates. Data are normalized to TBP. *, p < 0.05; **, p < 0.01; ***, p < 0.001; ****, p < 0.0001 by one-way ANOVA followed by Dunnett's multiple comparisons test. **B.** Schematic of the experimental design for the mouse study. Mice were injected with AAV8-hLRH-1 intravenously to induce human LRH-1 expression, then after two weeks were treated with five doses of 10CA over three days. **C.** Liver tissue from mice was isolated and analyzed by qRT-PCR to measure levels of human LRH-1. **D.** Heatmap of Nanostring results in mice expressing AAV8-hLRH-1 and treated with vehicle, 0.1, 1.0,

or 10.0 mg/ kg 10CA. The $\log_2$ fold changes (LFC) *versus* vehicle-treated mice are shown. **E.** Individual bar graphs from Nanostring showing downregulation of lipogenic genes in mice receiving AAV8-hLRH-1 but not in control (CTRL) mice. *, $p < 0.05$, **p, 0.01, by two-way ANOVA followed by Benjamini-Yekutieli False Discovery Rate (FDR) method, using an FDR threshold of 0.05.
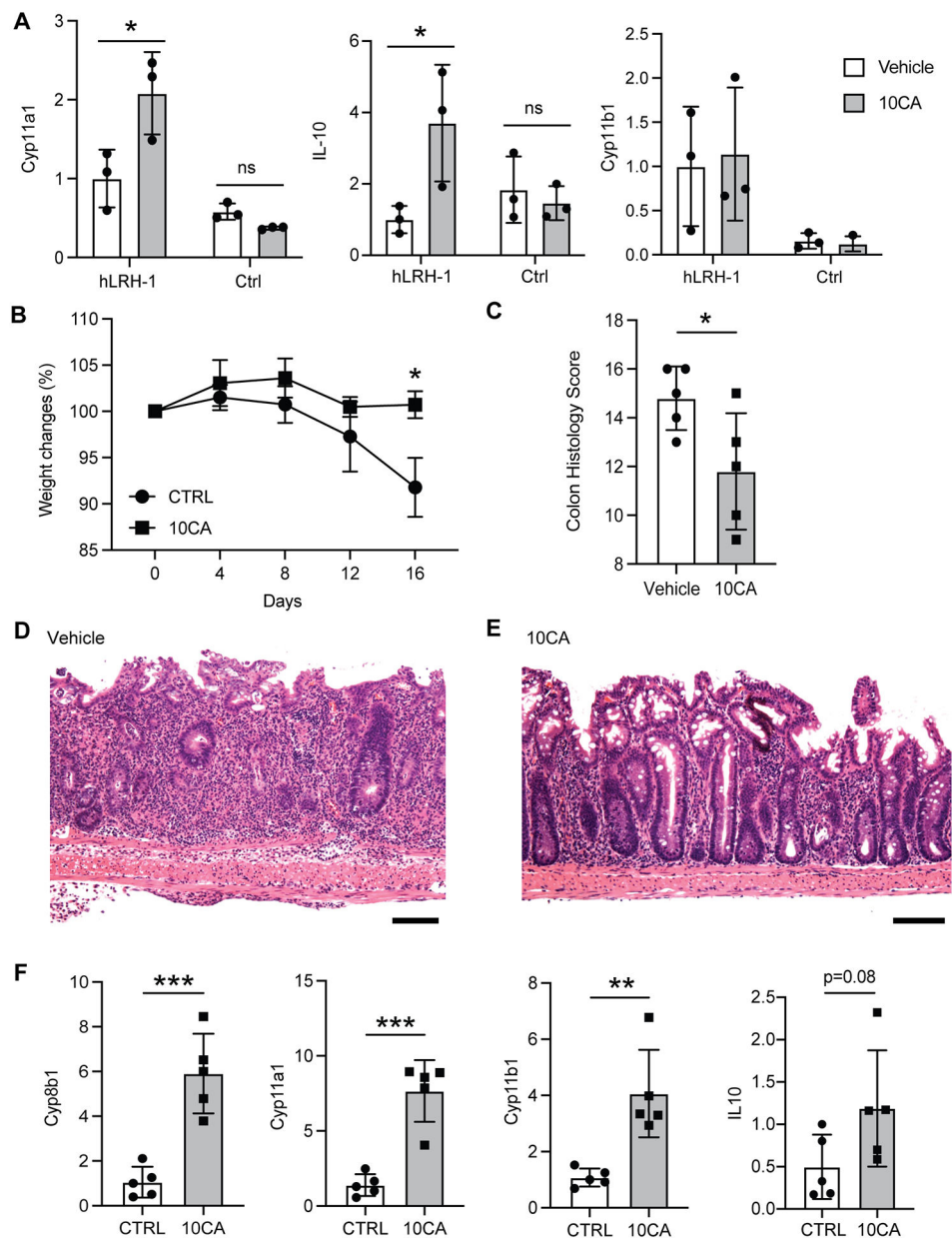
Figure 5. Efficacy of 10CA in models of intestinal inflammation and colitis.
A. Gene expression changes in enteroids treated with 10CA, measured by qRT-PCR (n = 3).
Bars represent the mean, error bars are standard deviation, and individual points are shown
from three replicates. Bars labeled "hLRH-1" denote enteroids expressing human LRH-1
in animals where mouse Lrh-1 was conditionally deleted in the intestinal epithelium. Bars
labeled "Ctrl" denote enteroids from epithelial-specific Lrh-1 knockout mice *, p < 0.05 by
two-way ANOVA followed by Sidak's multiple comparisons test. **B.** Plot of weight changes
of mice over the course of treatment in TCT experiment. Mice (n = 5) were treated six days
a week with vehicle (CTRL) or 10CA (20 mg/ kg). Each point represents the mean +/− SEM
from five mice per group. *, p< 0.05 (two-way ANOVA followed by the Bonferroni test
for multiple comparisons). **C.** Histology scores were calculated as described in the methods

section and Table S3. Each bar represents the mean, error bars are SD, and individual values are shown as points. **D-E.** Representative colon sections stained with H&E show reduced intestinal damage with 10CA treatment (*E*) compared to vehicle (*D*) Scale bars are 100 nm. **F.** qRT-PCR from of LRH-1 transcriptional targets in colonic crypts of mice from the TCT experiment. Each bar represents the mean, error bars are SD, and individual values are shown as points. *, $p < 0.05$, **, $p < 0.01$, ***, $p < 0.001$ relative to vehicle-treated organoids or mice by two-tailed, unpaired Student's t-test.

Table 1:

X-ray data collection and refinement statistics.

Data collection	LRH-1 + 10CA + TIF2	LRH-1 + 9ChoP + TIF2
Space group	P3$_2$21	P3$_2$21
Cell dimensions		
a, b, c (Å)	88.4, 88.4, 105.7	89.2, 89.2, 106.5
α, β, γ (°)	90, 90, 120	90, 90, 90
Resolution (Å)	38.27 – 2.30 (2.38 – 2.30)	34.21 – 2.55 (2.64–2.55)
R_{pim}	0.045 (0.305)	0.074 (0.542)
$I / \sigma I$	22.7 (1.79)	13.8 (1.31)
CC$_{1/2}$	97.0 (77.6)	98.7 (57.1)
Completeness (%)	99.8 (98.7)	99.9 (100.0)
Redundancy	15.8 (15.3)	13.8 (13.8)
Refinement		
Resolution (Å)	2.30	2.55
No. reflections	21639	16426
R_{work} / R_{free} (%)	18.9/ 22.7	17.6 / 20.1
No. atoms		
Protein	2037	2061
Water	38	18
Twin Law	n/a	-h, -k, l
B-factors		
Protein	66.3	63.7
Ligand	52.6	65.0
Water	60.2	49.7
R.m.s. deviations		
Bond lengths (Å)	0.002	0.001
Bond angles (°)	0.48	0.33
Ramachandran favored (%)	97.2	97.6
Ramachandran outliers (%)	0	0
PDB accession code	7JYD	7JYE

Values in parentheses indicate highest resolution shell.

KEY RESOURCES TABLE

REAGENT or RESOURCE	SOURCE	IDENTIFIER
Antibodies		
Penta-His Alexa Fluor 488 Conjugate	Qiagen	Cat# 35310
Bacterial and virus strains		
BL21(pLysS) *E. coli*	Agilent	Cat# 200132
BL21 (DE3) *E. coli*	Agilent	Cat# 200131
AAV8-ApoE/hAAT1-eGFP-WPRE	Vector Biolabs	Cat# VB2008
AAV8-ApoE/hAAT1-AVI-hLRH-1	Vector Biolabs	Cat# AAV-217060
Biological samples		
n/a		
Chemicals, peptides, and recombinant proteins		
Human Tif2 peptide H_3N-KENALLRYLLDK-CO_2^-	RS Synthesis	N/A
DLPC	Avanti Polar Lipids	Cat# 850335
Recombinant human LRH-1	This paper	N/A
Recombinant human LRH-1-LBD	This paper	N/A
6N-FAM	(D'Agostino et al., 2020)	N/A
Critical commercial assays		
Quikchange Lightning Site Directed Mutagenesis Kit	Agilent	Cat# 210518
Dual-Glo Luciferase Assay System	Promega	Cat# E2920
Deposited data		
LRH-1–10CA-Tif2 structure	This paper	PDB: 7JYD
LRH-1–9ChoP-Tif2 structure	This paper	PDB: 7JYE
LRH-1-DLPC-Tif2 structure	(Musille et al., 2012)	PDB: 4DOS
LRH-1-RJW100-Tif2 structure	(Mays et al., 2016)	PDB: 5L111
Experimental models: Cell lines		
Human: Hela cells	ATCC	RRID:CVCL_0058
Human: Huh7 cells	A gift from Paul Dawson, Emory University	RRID:CVCL_0336
Experimental models: Organisms/strains		

REAGENT or RESOURCE	SOURCE	IDENTIFIER
Mouse: C57BL/6J	Jackson Labs	Cat# 000664
Mouse: LRH-1 KO (LRH-1$^{f/f}$;Villin-Cre+) *source of LRH-1 KO enteroids*	Laboratory of David Moore (Bayrer et al., 2018)	N/A
Mouse: hLRH-1 (LRH-1$^{f/f}$;hLRH-1 ;Villin-Cre+) *Source of hLRH-1 enteroids*	Laboratory of David Moore (Bayrer et al., 2018)	N/A
Mouse; hLRH1^{IEC} (Rag2$^{-/-}$ hLRH1^{IEC-TG} mLRH1^{IEC-KO})	Laboratory of David Moore (Bayrer et al., 2018)	N/A
Oligonucleotides		
FAM-CYP7A1: 5'-GTTCAAGGCCAG-3' (forward strand of a DNA duplex labeled with FAM)	(Solomon et al., 2005)	N/A
Cyp11b1 qRT-PCR primers	QuantiTect	Cat# QT01198575
All other primers for qRT-PCR are shown in Table S4	Integrated DNA Technologies (IDT)	N/A
Recombinant DNA		
Plasmid: pMSC7 His-LRH-1_LBD	(Musille et al., 2012)	N/A
Plasmid: pMSC7 His-LRH-1_LBD^{Y516A}	This paper	N/A
Plasmid: pMSC7 His-LRH-1_LBD^{K520A}	This paper	N/A
Plasmid: PET28b His-SUMO-LRH-1	(Mays et al., 2017)	N/A
Plasmid: pGL3-SHP_RE-FireflyLUC	(Solomon et al., 2005)	N/A
Plasmid: pCMV-RenillaLUC	(Musille et al., 2012)	N/A
Plasmid: pCI empty vector	Promega	Cat# E1731
Plasmid: pCI-LRH-1	(Solomon et al., 2005)	N/A
Plasmid: pCI-LRH-1^{Y516A}	This paper	N/A
Plasmid: pCI-LRH-1^{K520A}	This paper	N/A
Plasmid: pCI-LRH-1^{A349F}	(Mays et al., 2016)	N/A
Software and algorithms		
Amber17	Amber	https://ambermd.org/
Phenix v1.16	(Adams et al., 2010)	https://phenix-online.org/
HKL2000	(Otwinowski, 1997)	https://hkl-xray.com/
Coot v0.8.9.2	(Emsley and Cowtan, 2004)	http://scottlab.ucsc.edu
Pymol v2.1.1	Schrodinger, LLC	www.pymol.org
GraphPad Prism v9	GraphPad	https://www.graphpad.com
RStudio v1.2.1335	R Core Team	https://www.rstudio.com/
nSolver v4.0	NanoString Technologies, Inc	https://www.nanostring.com
AmberTools17	Amber	https://ambermd.org/
ProteinLynx Global SERVER	Waters Corporation	https://www.waters.com/
DynamX v3.0	Waters Corporation	https://www.waters.com/
ChemDraw Professional 18.0	PerkinElmer	https://perkinelmerinformatics.com/products/research/chemdraw/

REAGENT or RESOURCE	SOURCE	IDENTIFIER
Other		